Universitat Politècnica de Catalunya

Department of Physics

Nonlinear Dynamics, Nonlinear Optics and Lasers (DONLL)

Doctoral thesis

HILBERT ANALYSIS OF AIR TEMPERATURE DYNAMICS

Author:
Dario Zappalà

Supervisor:
Prof. Cristina Masoller

Terrassa (Spain), 2019

Contents

Contents **iii**

Abbreviations **vii**

Abstract **ix**

Resumen **xi**

1 Introduction **1**
1.1 Overview of climate complexity 1
1.2 Analysis of climate time series 6
1.3 Plan of the thesis 8

2 Hilbert analysis **11**
2.1 Overview of the Hilbert transform 11
2.2 Limitations of the Hilbert transform 13
2.3 Datasets 14
2.4 Methods 15

3 Hilbert frequency of SAT time series **19**
3.1 Global statistics of frequency 20
3.2 Analysis of specific geographical sites 21
3.3 Alternative calculation of frequency 24
3.4 Seasonal behaviour of frequency 26
3.5 Discussion 27
3.6 Conclusions 29

4 Changes in SAT dynamics over the last 35 years **31**
4.1 Quantifying changes in SAT dynamics 32
4.1.1 Relative change 32
4.1.2 Significance analysis 33
4.2 Amplitude changes 33
4.3 Frequency changes 36
4.4 Conclusions 38
4.5 Appendices 39
4.5.1 Significance test 40
4.5.2 Influence of the time interval length 41
4.5.3 Comparison with NCEP-DOE dataset 44

5 Unveiling temporal regularities in SAT **47**
5.1 Dependence of the mean period on the smoothing length 48
5.2 Relation between phase and date of the year 50
5.3 Analysis of SAT dynamics 51
5.4 Classification of SAT dynamics 54
5.5 Conclusions 56
5.6 Appendices 57
5.6.1 Fourier analysis 57
5.6.2 Analysis of synthetic data 58
5.6.3 Comparison with NCEP-DOE dataset 60
5.6.4 Comparison with monthly SAT 62

6 Correlations and synchronisation in SAT time series **63**
6.1 Synchronisation 64
6.2 Linear correlation 65
6.2.1 Linear correlation without time lag 68
6.2.2 Linear correlation with time lag 70
6.3 Nonlinear correlation 70
6.4 Discussion 71

7 Conclusions **75**
7.1 Summary 75
7.2 Future perspectives 78

Bibliography **81**

Publications **93**

Conferences, workshops and research stays **95**

Abbreviations

ENSO	El Niño–Southern Oscillation
HT	Hilbert Transform
ITCZ	Intertropical Convergence Zone
SAT	Surface Air Temperature
SST	Sea Surface Temperature
QBO	Quasi-Biennial Oscillation

Abstract

The dynamics of the climate system plays a crucial role in the sustainability of life on Earth, and this motivates research to understand and characterise our climate and predict its evolution. In this thesis we focus on the dynamics of atmospheric temperature and analyse time series of surface air temperature using the Hilbert transform. This allows us to characterise the dynamics of temperature with time series of instantaneous amplitude, phase and frequency. Using these series as the basis of our analysis, we extract meaningful information about global patterns of temperature dynamics.

Firstly, we calculate maps of time-averaged frequency and of its standard deviation and uncover patterns that correspond to well-known climatic conditions: different amplitudes of the annual temperature cycle and regions of high precipitation. In addition, we study the dynamics of instantaneous frequency and phase in three geographical sites. The results reflect the main features of different climates, in particular the difference between the tropical and the extratropical climate.

Then, we use the Hilbert time series to quantify interdecadal changes in temperature dynamics (specifically, in the last 35 years). We find high changes of amplitude in the Arctic and in Amazonia, which are interpreted respectively as due to ice melting and precipitation decrease. We also uncover frequency changes in the Pacific Ocean that suggest a shift towards north and a widening of the atmospheric convection pattern known as the intertropical convergence zone.

Thirdly, we uncover temporal regularities in phase dynamics. We smooth (by doing a temporal average on a moving window) the temperature series, then we apply the Hilbert analysis and study how the mean rotation period of the Hilbert phase depends on the length of the averaging window. In this way, we discover different types of atmospheric dynamics and classify geographical regions according to the results of our analysis.

Finally, we analyse correlations between the phase, amplitude and frequency dynamics in different regions. We analyse phase synchronisation in three areas: the northern extratropics, the southern extratropics and the tropics. Then, we select several geographical sites and study the statistical correlations with the rest of the world, using the different Hilbert time series. We find that these correlations capture large-scale climatic patterns, such as El Niño–Southern Oscillation and Rossby waves.

Resumen

La dinámica del sistema climático tiene un papel crucial en la sostenibilidad de la vida en la Tierra y esto motiva la investigación para comprender y caracterizar nuestro clima y predecir su evolución. En esta tesis nos centramos en la dinámica de la temperatura atmosférica y analizamos series temporales de la temperatura superficial del aire utilizando la transformada de Hilbert. Esto nos permite caracterizar la dinámica de la temperatura con series temporales de amplitud, fase y frecuencia instantáneas. Utilizando estas series como base de nuestro análisis, extraemos información significativa sobre los patrones globales de la dinámica de la temperatura.

En primer lugar, calculamos mapas de frecuencia promediada en el tiempo y de su desviación estándar y descubrimos patrones que corresponden a condiciones climáticas bien conocidas: diferentes amplitudes del ciclo anual de temperatura y regiones de alta precipitación. Además, estudiamos la dinámica de frecuencia y fase instantáneas en tres ubicaciones geográficas. Los resultados reflejan las características principales de los diferentes climas, en particular la diferencia entre el clima tropical y el extratropical.

Luego, usamos las series temporales de Hilbert para cuantificar los cambios entre décadas en la dinámica de la temperatura (específicamente, en los últimos 35 años). Encontramos grandes cambios de amplitud en el Ártico y en la Amazonia, que se interpretan respectivamente como debidos a la fusión del hielo y a la disminución de precipitación. También descubrimos cambios de frecuencia en el océano Pacífico que sugieren un desplazamiento hacia el norte y un ensanchamiento del patrón de convección atmosférica conocido como zona de convergencia intertropical.

En tercer lugar, descubrimos regularidades temporales en las dinámicas de fase. Suavizamos (haciendo un promedio temporal en una ventana móvil) la serie de temperatura, luego aplicamos el análisis de Hilbert y estudiamos cómo el periodo medio de rotación de la fase de Hilbert depende de la longitud de

la ventana de promediado. De esta manera, descubrimos diferentes tipos de dinámica atmosférica y clasificamos las regiones geográficas según los resultados de nuestro análisis.

Por último, buscamos correlaciones entre las dinámicas de fase, amplitud y frecuencia en diferentes regiones. Analizamos la sincronización de la fase en tres áreas: los extratrópicos del norte, los extratrópicos del sur y los trópicos. Luego, seleccionamos varias ubicaciones geográficas y estudiamos las correlaciones estadísticas con el resto del mundo, utilizando las series temporales de Hilbert. Encontramos que estas correlaciones capturan patrones climáticos a gran escala, como El Niño–Oscilación del Sur y las ondas de Rossby.

Chapter 1

Introduction

The Earth's climate is of fundamental importance for the presence and sustainability of life. Climate changes can have profound socio-economic impacts [1] and trigger complex ecological adaptation mechanisms [2–5]. On a short time scale, extreme events such as floods, droughts or anomalous temperatures can produce negative effects on different aspects of our life [6]. These reasons motivate research aimed at understanding climate and its long-term variations [7–11]. There are different questions that research is trying to answer, for example: How to identify climate similarities and differences in different parts of the world? Which mechanisms are responsible for the climate phenomena that we experience? Is it possible to foresee extreme weather events? How is climate going to change in the short and long terms?

1.1 Overview of climate complexity

In the framework of climate study, climate is defined as the temporal average of weather conditions over long periods of time. Actually, climate is determined by many characteristic processes over a wide range of time scales and spatial scales [12]. Figure 1.1 is an artistic rendering that summarises what is known about power spectrum of climate variability at all the time scales that have been studied [13].

The peaks in the leftmost part of the spectrum, in the interval 10^3–10^6 years, are calculated from paleoclimatic proxy indicators. They represent the glaciation cycles, the alternation between colder and warmer temperatures that dominated the Quaternary era. Some of these peaks can be explained by an

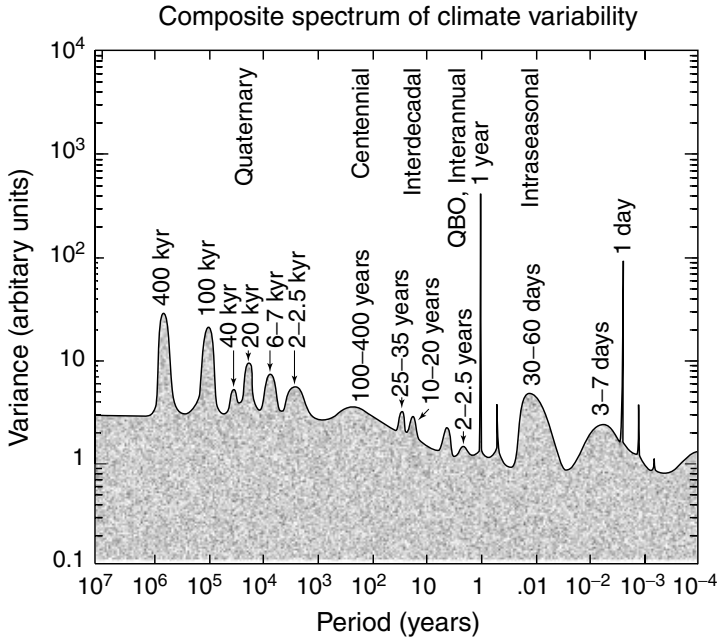

Figure 1.1: Artistic rendering of the power spectrum of climate variability on "all" time scales. It is obtained by putting together the spectral information calculated from many climatic series with different lengths and time resolutions. Taken from [13].

astronomical cause, i.e. variations in the Earth's orbit and axis of rotation; others can be explained by internal feedback loops between subsystems of the Earth's climate; and others still have an unclear origin [14, 15].

In the central range of the spectrum we find centennial (100–400 years), interdecadal (10–35 years) and interannual (2–5 years) oscillations. The interdecadal variability is particularly strong in the North Atlantic, due to the process known as *Atlantic Multidecadal Oscillation*. In particular, the northern North Atlantic undergoes a change in sea surface temperature on a time scale between 20 and 70 years. The interannual variability is produced by different processes, for example *El Niño–Southern Oscillation* (ENSO) and *Quasi-Biennial Oscillation* (QBO). In the next chapters, our analysis will find effects of this processes.

ENSO is an irregular fluctuation of sea surface temperature (SST) and air

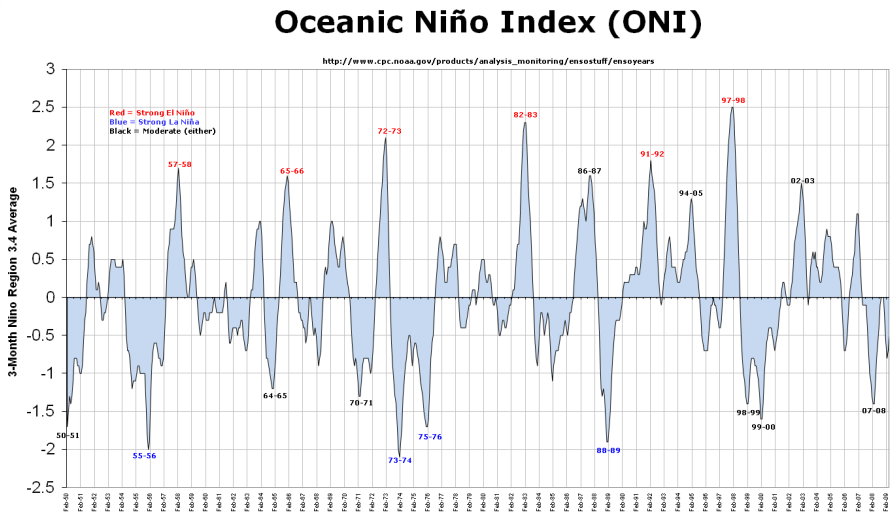

Figure 1.2: Oceanic Niño Index, obtained as a 3-month average of SST in the El Niño 3.4 region. Periods of El Niño are indicated in red, while periods of La Niña are indicated in blue. Taken from [18].

surface pressure on tropical Pacific Ocean [16, 17]. This fluctuation develops between three states: El Niño, La Niña and neutral. El Niño is the state in which the SST of eastern tropical Pacific increases by a few degrees. The associated fluctuation in the tropical atmosphere is called Southern Oscillation, and in the El Niño state there is lower surface pressure in the tropical eastern Pacific than in the western Pacific. Because of that, the low-level surface winds, usually blowing from east to west, get weakened or even blow in the opposite direction. In the La Niña state, the situation is opposite both in the sea and in the ocean: sea surface temperature in eastern tropical Pacific lowers and the usual westward winds over tropical Pacific get stronger. In the neutral state, SST and air surface pressure in the tropical Pacific region are close to average. We can see this oscillation in figure 1.2, which shows the evolution of the Oceanic Niño Index, representing the El Niño part of the oscillation [18]. The ENSO phenomenon is important because it deeply affects the weather not only in the tropical Pacific region, but also across the whole world [19–21].

QBO is a quasiperiodic oscillation, with a mean period of 28–29 months,

of the direction of zonal winds in the troposphere, that alternates between eastward and westward direction [22–25]. It has been shown that the main contribution to the production of QBO is given by gravity waves and this mechanism has been reproduced in different climate models [26–28]. In this thesis, we will see possible effects of QBO in an area in tropical Pacific.

In the right part of the spectrum of figure 1.1 we find the fastest variability modes. In particular, we can see two strong and narrow peaks: the annual and the daily oscillations, which are due to the change in solar radiation. The annual oscillation in solar radiation generates effects on different components of the system. For example, we can consider the *Intertropical Convergence Zone* (ITCZ), an area that encircles the Earth near the equator, where northern and southern trade winds converge [29]. The ITCZ moves according to the season: it shifts northward during northern summer and southward during southern summer. The change of the position of the ITCZ affects rainfall in many equatorial areas and causes a pattern of wet and dry seasons, instead of a pattern of cold and warm seasons that is characteristic of extratropical latitudes.

Between the annual and the daily peaks of the spectrum, we find a broader peak representing intraseasonal variability, with a time scale of 1–2 months, which is partially due to *Madden-Julian oscillation*, an eastward movement in the atmosphere above the tropical regions of Indian and Pacific oceans [30, 31].

The other peak at 3–7 days represents the synoptic variability, which determines the weather in the extratropical regions and is very important for weather forecasts. One of the important mechanisms determining weather at this time scale is given by *Rossby waves* [32, 33]. These waves are due to the polar jet streams, eastward winds located at an altitude of 9–12 km (tropopause), between Polar and Ferrel circulation cells. These jet streams separate polar cold air and tropical warm air. Influenced by the Coriolis force and pressure gradient, the jet streams assume a characteristic windy pattern with large meanders. This meandering pattern propagates eastward, even if at lower speed than the wind that actually flows in the jet stream. Also, it can happen that a meander gets so stretched that it detaches as a separate mass of cold or warm air. These air masses become low-strength cyclones (cold air) or anticyclones (warm air) and have a great influence on weather at mid-latitudes.

The presence of widely different temporal scales is a characteristic feature of complex dynamical systems. Figure 1.3 presents the processes and interactions that determine the climate system. It is composed by many subsystems, each one characterised by different processes that introduce different time scales into the climate system. We can think of these time scales as the response

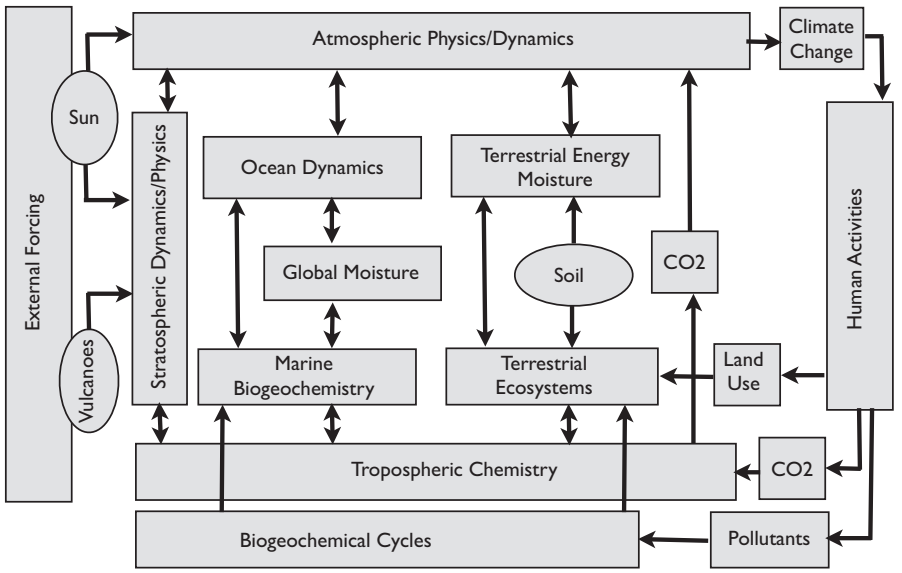

Figure 1.3: Representation of the complex organisation of the climate system. It shows the main subsystems and their interactions. Taken from [12].

time that a subsystem takes to go back to equilibrium after a perturbation [12]. Atmospheric responses, for example, have time scales that go from seconds (e.g., the formation of cloud droplets) to around a week (e.g., dissipation of midlatitude weather systems). Oceanic responses have longer time scales, from months (e.g., upper layers ocean mixing) to thousands of years (e.g., deep ocean circulation). The cryosphere (the frozen water part of the Earth's surface) has even a wider time range, with sea ice having shorter time scales than land ice. The biosphere (the sum of all the ecosystems on the Earth) also has a very wide time range, from seconds (respiration and photosynthesis) to millions of years (changes in biochemistry of living organisms due to evolution). The lithosphere (the solid outer layer of the Earth) has time scales that go up to millions of years (e.g., motion of continents).

Besides, interactions between the components of the climate system can introduce additional time scales. One of the most important examples is the phenomenon of El Niño, where the coupling between the equatorial ocean and the global atmosphere introduces a time scale of variability of about 3–7 years

[16, 17].

1.2 Analysis of climate time series

To advance in the understanding of our climate system, models with different levels of complexity can be used [34, 35]. While simple models only provide a good understanding of basic phenomena, state-of-the-art models allow for unprecedented predictability [36]. However, the complexity of these models can obscure the interpretation of their predictions.

In the last two decades, the availability of satellite data and advances in data mining [37] have lead to the use of data-driven approaches to understand, characterise and predict our climate. There are approaches based on classical statistics and bootstrap methods, to estimate the evolution of a given climatic variable within a confidence interval [38]. In addition, approaches based on complex networks and machine learning have been recently used to analyse climate data [39–46].

In the research work that is summarised in this thesis, we focus on the study of surface air temperature (SAT) time series. In particular, we take our data from reanalysis datasets. It means that, since observations are not available uniformly in time and space, climate models and data assimilation techniques are used to cover the gaps and provide data which is regularly sampled both in time and in space.

Univariate analysis tools that have been used to analyse SAT time series include detrended fluctuation analysis [47, 48], fractional analysis [49] and wavelet analysis [50, 51]. Changes in the SAT annual cycle have also been investigated, and a trend toward reduced cycle amplitude has been detected in many regions [52–58].

A successful approach to study climate is that of *climate networks*, given by the application of complex network theory to climate [19–21, 39, 59–65]. In this approach, climate data is available on a regular grid on the Earth's surface, whose points are taken as the vertices of the climate network. Bivariate analysis is performed on the climate time series of all the pairs of points: depending on the statistical significance of the correlation between the two points, the corresponding edge is added or not to the climate network. A common technique is to extract anomaly time series from the original climate time series, to remove the effect of annual cycle and consider only the deviations from that cycle. With the climate network approach it is possible to get meaningful information about the climate system at various spatial scales: from local properties (such as the

number of first neighbours of a vertex) to global properties (such as the clustering coefficient and average path length). An important role is played by the so-called supernodes (or hubs), vertices with a high number of first neighbours, which are associated to known dynamical interrelations in the atmosphere. In particular, supernodes are linked not only to nearby geographical regions, but also to distant regions. The latter links are called teleconnections. Climate networks have been found to have properties of small-world networks as well as scale-free networks, where supernodes correspond to major teleconnection patterns. Also, it has been found that teleconnections make climate more stable and make the climate network more efficient in transferring information [59, 60].

One of the tools that have been used to study geophysical time series is the Hilbert transform (HT). It provides, for an oscillatory time series, an analytic signal from which instantaneous amplitude, phase and frequency can be derived (see chapter 2). For this reason, the HT has been used to investigate a wide range of oscillatory signals [66–74]. In particular, the HT has been used to study various geophysical time series [75], since they show some degree of periodicity due to seasonality. For example, in [76] the HT was used to characterise the daily variability of the Seine river flow from 1950 to 2008, uncovering linkages between river flow variability and global climate oscillations (the North Atlantic Oscillation and the Madden-Julian Oscillation). In [77] the HT was used to compute the daily phase shift between temperature signals recorded at the ground surface and at a depth of 5 m in two meteorology stations in Taiwan from 1952 to 2008. Significant reductions in the phase shift from the 1980s to 1990s were found, a result which was interpreted to be related to the warming of the Pacific Decadal Oscillation. In [78], the HT was used to study rainfall time series in India and it was found that the multi-scale components of rainfall series have a similar periodic structure as global climate oscillations (QBO, El Niño–Southern Oscillation, etc.).

The Hilbert transform has not been used yet, to the best of our knowledge, to analyse SAT time series. Since SAT typically has a degree of seasonal periodicity (for example, extratropical sites are dominated by the annual cycle), the HT is a promising tool to study SAT. For this reason, in this thesis we develop techniques of analysis of SAT time series that are based on the HT.

Applying the HT to climate time series means, ultimately, that we are considering the time series as oscillations. In this case, it makes sense to measure the synchronisation within a set of oscillators, i.e. between all the time series of a certain geographical region. A classical tool to measure the synchronisation of oscillators is the *Kuramoto parameter*, introduced in the

framework of the Kuramoto model of coupled oscillators [69, 79, 80]. This model, with different variations, has found widespread applications in many fields, such as chemical oscillators, laser arrays, neural networks and Josephson junctions [81, 82].

We will show that the HT allows us to extract meaningful information about SAT dynamics, to characterise climate in different regions, to identify and to quantify climate changes and to calculate correlations that capture actual climate phenomena. The HT provides additional information, complementary to the one that can be obtained by using the many existing approaches [83]. Therefore, it is an important tool to advance the understanding of atmospheric temperature dynamics.

1.3 Plan of the thesis

In the next chapters we present the results of our studies that explore the potential of the HT to analyse climate time series, more specifically SAT series. Our presentation proceeds according to the following structure:

- In chapter 2 we describe the Hilbert transform, pointing out its possibilities and limitations. We also explain how we apply the HT to SAT time series.
- In chapter 3 we analyse spatial properties of instantaneous frequency of SAT. We show maps of average frequency, containing patterns which reflect different climatic regions. In addition, we study the SAT behaviour of relevant sites by analysing the Hilbert trajectories and the distribution of instantaneous frequency.
- In chapter 4 we use Hilbert analysis to quantify the changes in SAT dynamics, on a global scale, that have occurred over the last 35 years. Hilbert amplitude shows the highest changes in the Arctic and in Amazonia, which can be interpreted respectively as due to ice melting and precipitation decrease. We also find a pattern of frequency change that is compatible with the widening and northward shift of the intertropical convergence zone.
- In chapter 5 we present a novel method for extracting information from climatic oscillatory signals. We smooth the SAT series and then apply the Hilbert analysis. We calculate the dependence of the mean rotation period of the Hilbert phase on the smoothing length. By analysing this dependence, we are able to characterise different climatic regimes. In

addition, we can use this dependence as the input of a classification algorithm, to identify different climatic regions.

- In chapter 6 we study the climate system from the point of view of a complex system of coupled oscillators. We calculate the Kuramoto parameter in three different regions, finding strong synchronisation in the extratropics and weak synchronisation in the tropics. Then, we calculate statistical correlations using different time series: SAT anomaly and series that we calculate by Hilbert analysis. Analysing the correlations between different geographical sites given by these series, we uncover various climatic properties, such as the effects of Rossby waves.

Chapter 2

Hilbert analysis

In this chapter we explain how we calculate the Hilbert transform and use it to analyse SAT data. Firstly, in section 2.1 we illustrate the Hilbert transform and its properties. In section 2.2 we illustrate the main limitations of the HT and some methods to overcome them. Then, in section 2.3 we describe the datasets that we use in our work. Lastly, in section 2.4 we explain how, starting from SAT time series, we can calculate the time series of amplitude, phase and frequency.

2.1 Overview of the Hilbert transform

The Hilbert transform is a linear operator that transforms a real signal $x(t)$ into another real signal, indicated by $H[x](t)$. It is defined as the convolution of $x(t)$ with the function $1/(\pi t)$:

$$y(t) = H[x](t) = \frac{1}{\pi}\text{p.v.}\int_{-\infty}^{+\infty}\frac{x(\tau)}{t-\tau}d\tau, \tag{2.1}$$

where p.v. indicates the Cauchy principal value. The HT allows us to define a complex *analytic signal* $h(t)$, from which an instantaneous amplitude and an instantaneous phase can be calculated:

$$h(t) = x(t) + iy(t) = A(t)e^{i\varphi(t)}. \tag{2.2}$$

The amplitude $A(t)$ and the phase $\varphi(t)$ can be calculated as

$$A(t) = \sqrt{[x(t)]^2 + [y(t)]^2}, \tag{2.3}$$

$$\varphi(t) = \arctan \frac{y(t)}{x(t)}. \tag{2.4}$$

These two quantities allow to reconstruct the original signal as

$$x(t) = A(t) \cos \varphi(t). \tag{2.5}$$

Besides, we can also calculate the time derivative of the phase to obtain the frequency, $\omega(t)$. We can use these new signals, obtained by using the HT, to characterise different types of oscillating signals. Analogous calculations can be done for signals $x(t)$ with discrete time, as is the case of this thesis work.

As a first example, the Hilbert transform of the harmonic oscillation $x(t) = A\cos(\omega t)$, where ω is a real positive constant, is $y(t) = A\sin(\omega t)$. In the complex plane, $(x(t), y(t))$ represent the coordinates of a point that describes a circular trajectory of amplitude A and phase ωt. In general, for an arbitrary signal $x(t)$, the Hilbert transform produces a new signal $y(t)$ where each spectral component has a $-\pi/2$ phase shift with respect to the original signal.

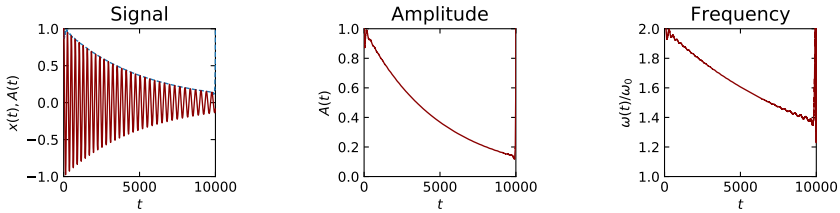

Figure 2.1: Hilbert analysis applied to the signal with time-varying amplitude and frequency given by equation 2.6. The first panel shows the signal $x(t)$ (red line) and its Hilbert amplitude $A(t)$ (blue dashed line); the second panel shows only the Hilbert amplitude $A(t)$; the third panel shows the ratio between the instantaneous Hilbert frequency and ω_0.

As a second example, we consider a signal with discrete time, that oscillates according to

$$x(t) = \mathrm{e}^{-2\alpha t} \cos\left[\left(1 + \mathrm{e}^{-\alpha t}\right) \omega_0 t\right]. \tag{2.6}$$

Its length is $L = 10^4$. We choose $\omega_0 = 2\pi/500$ (which would describe an oscillation of length 500 in a harmonic oscillator) and $\alpha = 1/L$. We calculate

the HT and then the instantaneous amplitude and frequency. The results are shown in figure 2.1. We can see that the amplitude $A(t)$ is the exponentially decreasing envelope of the signal $x(t)$, given by the expression $\mathrm{e}^{-2\alpha t}$, while the frequency $\omega(t)$ decreases according to $(1 + \mathrm{e}^{-\alpha t})\,\omega_0$. We also note that, near the extremes, $A(t)$ and $\omega(t)$ display an oscillatory behaviour that deviates from the exact analytical expressions.

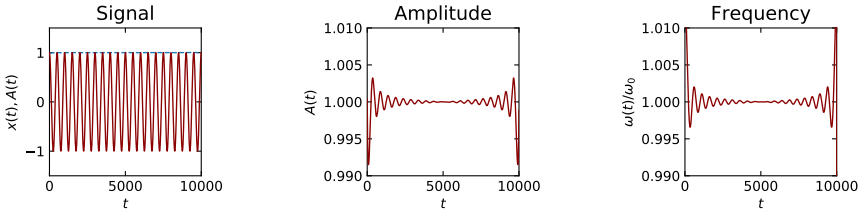

Figure 2.2: As figure 2.1, but for the harmonic signal $x(t) = \cos(\omega_0 t)$.

To better understand the magnitude of this effect, we take into account a simple harmonic oscillation $x(t) = \cos(\omega_0 t)$, again with length $L = 10^4$ and $\omega_0 = 2\pi/500$. In figure 2.2 we show the results of Hilbert analysis applied to this signal. We see that the amplitude $A(t)$ is the envelope of the signal $x(t)$. However, a closer inspection (in the second panel) reveals small oscillations near the extremes of the time domain. In the same way, the instantaneous frequency $\omega(t)$ is not always exactly equal to the theoretical frequency ω_0, since it displays oscillations near the extremes. In general terms, the Hilbert transform applied to a finite-time signal produces these oscillating errors near the extremes of the signal. Even if the reconstruction $x(t) = A(t)\cos\varphi(t)$ still exactly holds, the values of amplitude, phase and frequency, taken separately, deviate from the true values that we know from the model.

2.2 Limitations of the Hilbert transform

Although formally the instantaneous amplitude, phase and frequency can be computed for any arbitrary signal $x(t)$, they have a clear physical meaning only if $x(t)$ is an oscillatory signal with a narrow band of frequency. In this case, the amplitude $A(t)$ coincides with the envelope of $x(t)$ and the frequency $\omega(t)$ coincides with the frequency of the maximum of the power spectrum computed in a running window (see appendix A2 in [69] for a detailed discussion).

On the other hand, the instantaneous amplitude, phase and frequency lack a clear physical meaning when the signal is a superposition of oscillating components with different time scales. This is indeed a common situation in real-world oscillations and particularly relevant for climatic time series [84]. Huang and coworkers [66, 75, 85] have proposed and compared different methods to overcome this limitation of the Hilbert analysis. A well-established method is the empirical mode decomposition, that breaks down the original signal into a set of intrinsic mode functions. Each one of these functions admits a "well-behaved" Hilbert transform and is fully characterised by instantaneous amplitude and phase with the physical meaning of a rotation. Another solution is to apply a band-pass filtering, to isolate a narrow frequency band, and then apply the HT to the filtered signal.

However, even in datasets that do not meet the mathematical requirements to ensure well-behaved signals, the results of Hilbert analysis (as well as of other nonlinear analysis tools [86]) can be helpful for understanding and characterising the dynamical system that generates the signal. In the research work that we summarise in this thesis, in some cases we apply a smoothing filter before the HT and in other cases we directly calculate the HT of the raw data. We will see that in both cases we can obtain meaningful and useful information.

2.3 Datasets

In our work we mainly use the ERA-Interim reanalysis dataset [87], but to check the robustness of our findings we also compare them with the ones obtained from NCEP-DOE AMIP-II Reanalysis [88].

ERA-Interim gives information in regular grid of points over the Earth's surface, with a spatial resolution of 2.5 degrees, both in latitude and in longitude. That means that we consider $N = 73 \times 144 = 10512$ geographical sites. To indicate a site, we use an index $j \in [1, N]$. Since the sites are regularly spaced in latitude and in longitude, they are denser near the poles than near the equator. In other words, to each site corresponds an area which is proportional to the cosine of the latitude, so it is maximum at the equator and minimum at the poles. Thus, we assign to each site j the weight w_j, that is proportional to the area of the site:

$$w_j = \cos(\mathrm{lat}(j)). \tag{2.7}$$

For each site, we know the time series of SAT with daily resolution, from 1979 to 2017. So, every SAT time series has a length of $L = 14245$ days.

NCEP-DOE AMIP-II Reanalysis covers a longer time interval than ERA-Interim, over a grid of $94 \times 192 = 18048$ geographical sites. In order to perform a precise comparison between the results of the two datasets, in NCEP-DOE we consider the same time interval as in the ERA-Interim dataset.

The two reanalysis datasets analysed in this thesis are freely available at [89, 90].

2.4 Methods

Figure 2.3 describes the steps taken to obtain the Hilbert time series of instantaneous amplitude, phase and frequency from a SAT time series. To explain the procedure, we choose a geographical site that is located in continental east Asia and that will be shown to have a "regular" behaviour.

To indicate the raw SAT time series we use the notation $r_j(t)$, where $j \in [1, N]$ indicates the site and $t \in [1, L]$ indicates the day. First, we smooth the series by taking a moving temporal average of $r_j(t)$ over a window of length τ. In figure 2.3 we show the results for $\tau = 1$ day, i.e. no smoothing. Then, we remove the linear trend and normalise the time series to zero mean and unit variance. The preprocessed (smoothed, detrended and normalised) time series is referred to as $x_j(t)$. Since we consider this series as an oscillating signal, we apply to it the Hilbert transform for discrete time to obtain the complementary oscillation $y_j(t) = H[x_j](t)$. Specifically, we use the Hilbert function of the SciPy library of Python. We can see these two time series as the coordinates of a point that describes a "noisy circle" trajectory. The first three panels of figure 2.3 represent the preprocessed SAT series $x_j(t)$, its Hilbert transform $y_j(t)$ and the trajectory described by the two time series.

We anticipate here that the case shown in the picture is the "regular" case, in which the noisy circle is well defined, since its amplitude is bigger than the irregular fluctuations. Therefore, instantaneous amplitude and phase, $A_j(t)$ and $\varphi_j(t)$, can be defined and it's easy to see the meaning of equations 2.3 and 2.4 to calculate them. We will also see that, even in "irregular" cases where amplitude and phase could not be defined with a rotation meaning, the Hilbert analysis is nevertheless able to find meaningful results. Taking into account the individual signs of $x_j(t)$ and $y_j(t)$, we can obtain $\varphi_j(t)$, measured in radians, in the interval $[-\pi, \pi]$. As a general trend, when the increasing phase reaches the upper extreme of this interval, then it jumps to the lower extreme and starts to grow again. We eliminate these sudden jumps using a standard function (in the NumPy library of Python) that appropriately adds multiples of 2π. By doing

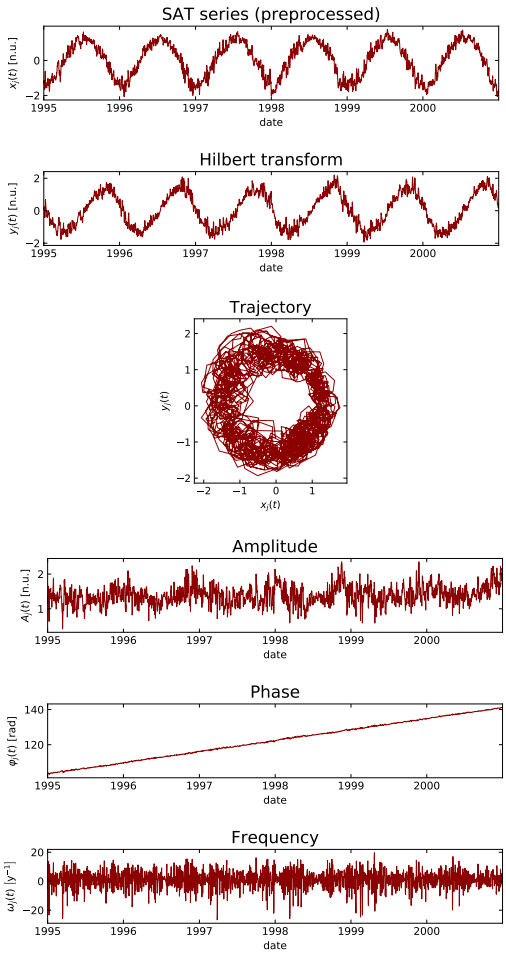

Figure 2.3: Computation of the Hilbert time series for a site in continental east Asia. For easy visualisation, we limited the plots to the period 1995–2000.

this, we unwrap the phase and obtain a "continuous" evolution in time. For example, if the SAT series is dominated by the annual oscillation, we expect the phase to have an increasing trend of 2π per year.

Then, we obtain the instantaneous frequency series, $\omega_j(t)$, as the time derivative of the unwrapped phase, using a second-order discrete formula. In the case of the annual oscillation, we expect the frequency to have the value of $1\,\mathrm{y}^{-1}$. The last three panels of figure 2.3 show the amplitude $A_j(t)$, the phase $\varphi_j(t)$ and the frequency $\omega_j(t)$. Calculations show, as expected, that the phase has an average evolution of 2π in one year and that the frequency, while having large fluctuations, has an average value of $1\,\mathrm{y}^{-1}$.

In this thesis work, we compare results obtained by Hilbert time series (amplitude, phase and frequency) with results obtained by other approaches. A popular approach in climate studies is to decompose the SAT time series into two components: climatology and anomaly. Climatology represents the typical yearly evolution of the time series and is calculated, for each day of the year, as the average over all the years of the SAT time series. Anomaly is the deviation of actual SAT, $r_j(t)$, from climatology and is calculated simply as the difference between the two quantities. We indicate climatology with $c_j(t)$ and anomaly with $z_j(t)$. So, anomaly is calculated as

$$z_j(t) = r_j(t) - c_j(t). \tag{2.8}$$

As we explained in section 2.2, the HT algorithm applied to a finite-time series produces fluctuating errors near the extremes in each of the calculated series. After testing with various examples, by comparing the numerical HT with the known analytical HT, we choose to discard the initial and final 2 years from the final Hilbert series, so that they have a relative error which is lower than 10^{-2}. In this way, we analyse time series of 35 years (from 1981 to 2015) with length $L = 12783$ days.

Chapter 3

Hilbert frequency of SAT time series

In this chapter we explore the potential of the Hilbert transform to analyse SAT time series. In each geographical site, annual solar forcing and atmospheric variability give different contributions to, respectively, a regular oscillation and a noisy background. Our work is aimed at studying the properties of SAT oscillations by means of the HT. Depending on the site, the Hilbert trajectory can be a "noisy limit cycle", with well-defined amplitude and phase, or it can have a more irregular behaviour. Analysing the frequency and the trajectory on a global scale, we aim to address the following questions: is it possible to quantify the degree of regularity of SAT dynamics by means of the statistical properties of the Hilbert frequency time series? Can we identify geographical regions with regular frequency dynamics and other regions with strongly fluctuating frequency? Does frequency behaviour change according to seasons?

To address these issues, we consider SAT data from ERA-Interim dataset. For each site we calculate the frequency series from the SAT series, as explained in chapter 2, without applying any filter to raw SAT. In spite of the fact that the analysed SAT series have a "non-monochromatic" and a "not narrow band" nature (and thus do not meet the mathematical conditions needed to obtain a Hilbert phase with a physical meaning of rotation), we show here that HT applied to them gives meaningful results, that can help us to characterise SAT dynamics.

As it was shown in figure 2.3, the instantaneous frequency can have large fluctuations. Here we show that the maps of time-averaged frequency and

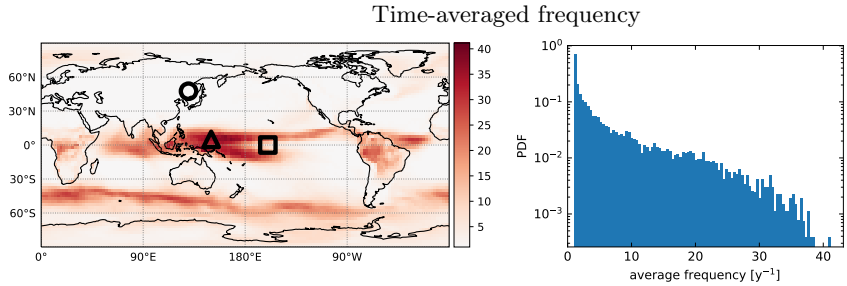

Figure 3.1: Global distribution of time-averaged frequency. The left panel shows the map of time-averaged frequency. Its colour scale is in units of y^{-1} and is adjusted so that the frequency value corresponding to the annual cycle ($1\,y^{-1}$) is displayed in white. The circle, triangle and square indicate the following geographical sites: northern extratropics (47.5 N, 130 E), western Pacific (5 N, 150 E) and central Pacific (0 N, 160 W). The right panel shows the histogram of time-averaged frequency of all the sites, weighted according to the area of each site.

its standard deviation present large-scale coherent structures with regions of regular or irregular frequency dynamics, which can be interpreted in terms of large-scale atmospheric phenomena. In the extra-tropics, the average frequency in general corresponds to the expected one-year period of solar forcing, while in the tropics a different behaviour is found, with particular regions having a faster average frequency. In the standard deviation map, large-scale structures are also found, which tend to be located over regions of strong annual precipitation.

Section 3.1 presents histograms and maps of time-averaged frequency and its standard deviation. In section 3.2 we analyse in detail three sites with different behaviours. Then, in section 3.3 we use another method to calculate frequency, to test the robustness of our results. Finally, in section 3.4 we analyse how frequency changes between summer and winter.

The results that we present in this chapter were published in [91].

3.1 Global statistics of frequency

We perform a statistical analysis of the obtained time series of instantaneous frequencies: for each site j, we calculate the time-averaged value of the frequency, $\overline{\omega}_j$, and its standard deviation, σ_j, and show with colour maps how these values are distributed over the world.

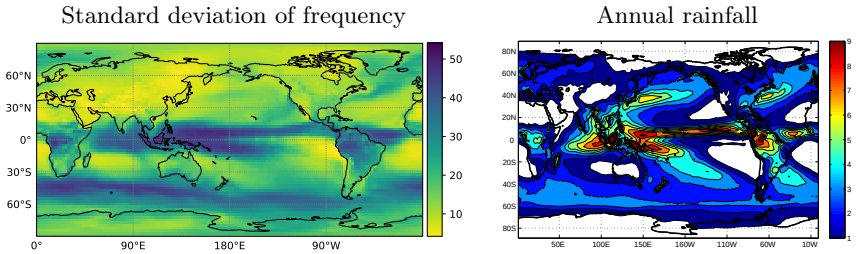

Figure 3.2: The left panel shows the map of standard deviation of instantaneous frequency, where the colour scale is in units of y^{-1}. The right panel shows the map of annual mean precipitation in units of mm/day (we reproduced this figure using data from The Version 2 Global Precipitation Climatology Project (GPCP) [92]).

We begin by presenting the plot of the spatial distribution of time-averaged instantaneous frequency in figure 3.1. In the map, the colour code represents the averaged frequency in units of y^{-1}, and is adjusted so that white corresponds to the frequency of the annual cycle ($1\,y^{-1}$), while red represents higher frequency values. Large scale structures are seen, with well-defined geographical regions where the average frequency is faster than the annual cycle. The histogram shows the distribution of time-averaged frequencies, weighted according to the area of each site. Its peak corresponds with the frequency of the annual cycle.

To investigate the spatial structure of frequency fluctuations, figure 3.2 displays in colour code the map of the standard deviation of the frequency series and compares it to the map of annual mean precipitation [92]. We will discuss the similarities and differences between these maps.

3.2 Analysis of specific geographical sites

As a second step, we choose three sites with different SAT behaviours and analyse in detail their Hilbert trajectory and their instantaneous frequency.

Figure 3.3 gives details about a site located in the extratropics, in continental east Asia, indicated in figure 3.1 with a circle in a white area. The instantaneous frequency and the corresponding trajectory are shown, during a the period 1995–2000. Additionally, the frequency pdf is shown, computed with all the values in the time series. Since a "regular" SAT dynamics in the extratropics consists of an annual four-season oscillation (with relatively small fluctuations due to SAT variability), we expect an average instantaneous frequency equal to

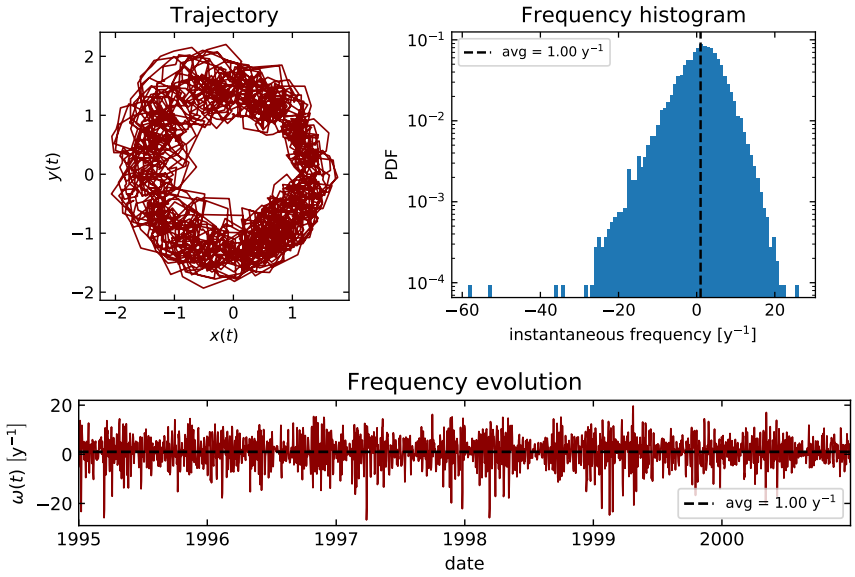

Figure 3.3: Analysis of the site located in the northern extratropics (indicated in figure 3.1 with a triangle). The upper left panel shows the Hilbert trajectory. The upper right panel shows the histogram of instantaneous frequency. The lower panel shows the evolution of instantaneous frequency. In the two panels of instantaneous frequency, the dashed line indicates the average value. For ease of view, trajectory and frequency evolution are plotted only in the period 1995–2000.

one rotation per year. In fact, looking at the data presented in figure 3.3, we see that the average instantaneous frequency corresponds to the expected value. We also note the presence of negative values of the instantaneous frequency and we remark that the histogram covers a wide range of both positive and negative frequency values (i.e. clockwise and anticlockwise rotation). We will show later that this is in part due to the fact that we are not applying any filter to the signal. While other methods can be employed to obtain an always positive frequency (see [69] for a discussion), we will show that this simple approach yields meaningful information about large-scale patterns in SAT dynamics. We also remark that, in this typical "regular" case, the trajectory shows a well-defined noisy limit cycle, since its amplitude is bigger than the irregular fluctuations; therefore, the instantaneous phase is always defined.

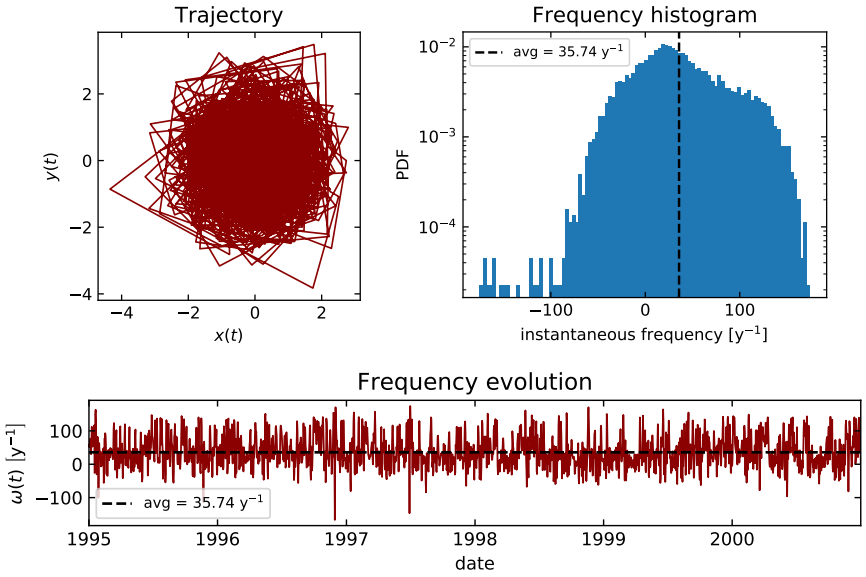

Figure 3.4: Analysis of the site located in the western Pacific (indicated in fig. 3.1 with a triangle). Analogous to fig. 3.3.

Next, we discuss two examples of "faster" sites, with "irregular" trajectories that do not resemble noisy limit cycles. We will show that the "irregular" behaviours are clearly captured by Hilbert frequency analysis. Figure 3.4 shows the same analysis performed on a site located in the western Pacific Ocean, indicated in figure 3.1 with a triangle in a red area. A highly irregular dynamics is observed, which does not resemble a noisy limit cycle, and the fluctuations of the instantaneous frequency are larger than those in a regular site (compare the histograms of the two figures 3.3 and 3.4).

Figure 3.5 shows analogous results for a site located in the central Pacific Ocean, indicated in figure 3.1 with a square in a transition area (at the border of a red area). Here again we observe a highly irregular dynamics, but in contrast with the previous case, the frequency fluctuations are usually small, and only occasionally there are large fluctuations.

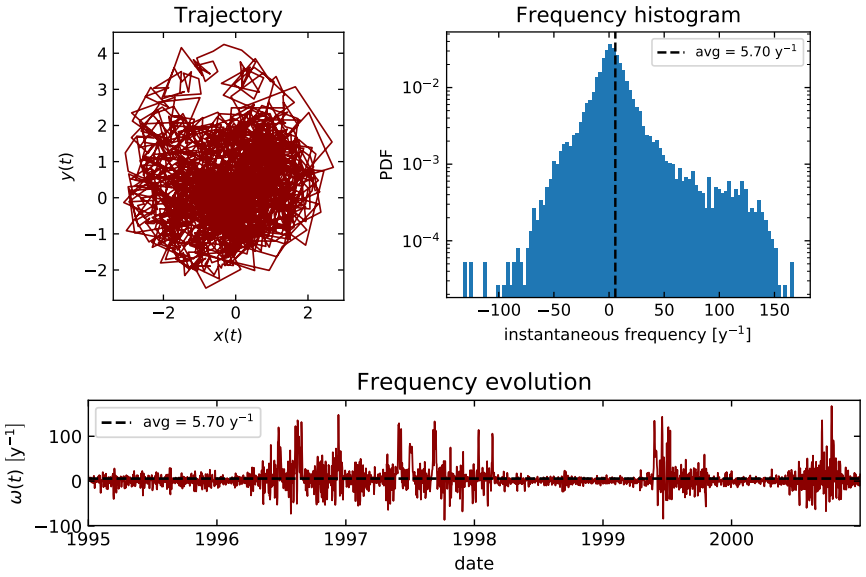

Figure 3.5: Analysis of the site located in the central Pacific (indicated in fig. 3.1 with a square). Analogous to fig. 3.3.

3.3 Alternative calculation of frequency

To test the robustness of our results, we calculate the frequency in a different way: we divide the time series of the phase, $\varphi_j(t)$, in windows of 31 days and then we calculate the slope of the linear regression of the phase in each window. In other words, the Hilbert frequency is computed as the linear trend of the phase in windows of 31 days. So, we have a value of frequency for each 31-day window and we can calculate statistics over these values. The obtained results are presented in figure 3.6: we see that the map of average frequency and the histogram of average frequency (the two upper panels) are almost identical to the ones in figure 3.1. On the other hand, the map of the standard deviation (lower panel) is qualitatively very similar to the one in figure 3.2 (it has the same spatial structures), but the standard deviation values are lower.

In contrast, the distribution of instantaneous frequency in the chosen sites changes drastically: negative values are almost fully suppressed. Figure 3.7

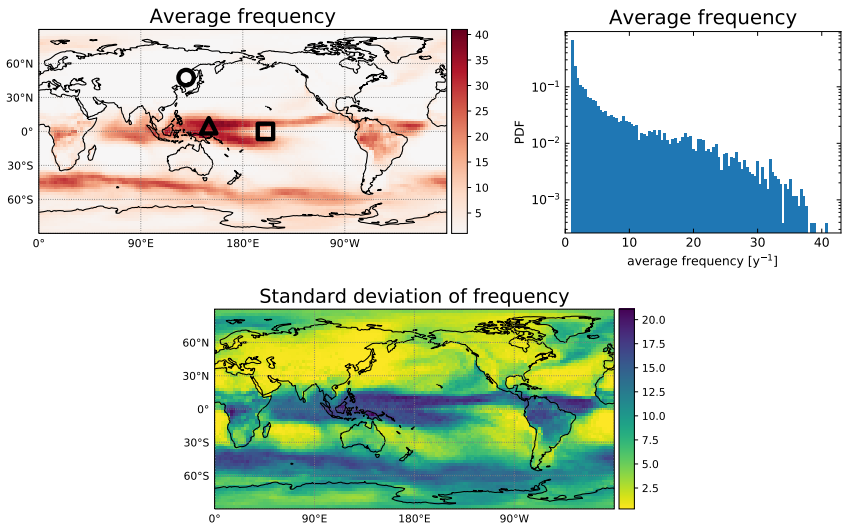

Figure 3.6: Hilbert frequency calculated as the linear trend of the phase in windows of 31 days. The upper left panel shows the map of time-averaged frequency, with the colour scale in units of y^{-1}. The upper right panel shows the histogram of time-averaged frequency of all the sites, weighted according to the area of each site. The lower panel shows the map of standard deviation of instantaneous frequency, with the colour scale in units of y^{-1}.

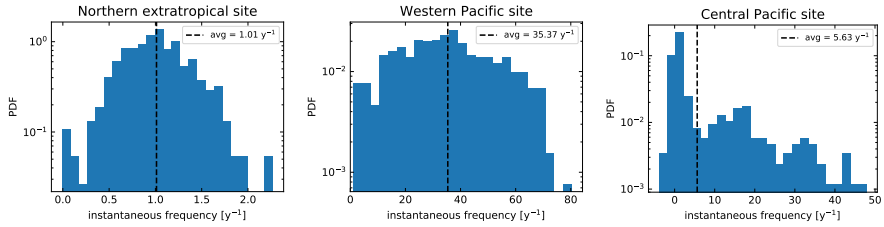

Figure 3.7: Histograms of instantaneous frequency calculated as the linear trend of the phase in windows of 31 days. The three panels show the histogram for the three chosen sites, indicated with a circle, a triangle and a square in figure 3.6.

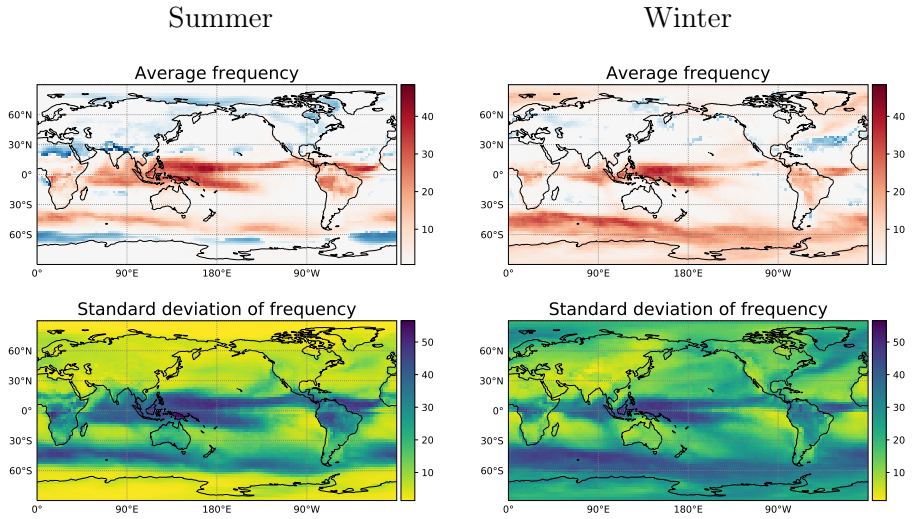

Figure 3.8: Results obtained by selecting summer (left column) or winter (right column) in the frequency series. The four panels show the maps of time-averaged frequency (upper row) and standard deviation of frequency (lower row). The colour scales are in units of y^{-1}. In the maps of average frequency, the blue colour indicates frequencies lower than $1\,\mathrm{y}^{-1}$.

shows the histograms of instantaneous frequency for the same sites as before (indicated with a circle, a triangle and a square in figure 3.6).

3.4 Seasonal behaviour of frequency

Lastly, in order to investigate how frequency fluctuations vary in different seasons, we extract from every time series of frequency, $\omega_j(t)$, the values that occur during winter and the ones that occur during summer (taking into account that winter in the northern hemisphere corresponds to summer in the southern hemisphere, and vice versa). In this way, for each site we obtain two series: one of winter frequency $\omega_j^{\mathrm{w}}(t)$, and one of summer frequency $\omega_j^{\mathrm{s}}(t)$. Then, we analyse the average value and the standard deviation of the two series. The results are displayed in figure 3.8. Remarkably, in the maps of average frequency we see large regions (blue colour) where frequency is lower than $1\,\mathrm{y}^{-1}$. These regions were not detected when analysing the whole frequency series (figure 3.1). The

maps of standard deviation show that frequency fluctuations in the extratropics are stronger in winter than in summer.

3.5 Discussion

As indicated before, the expected value of frequency (corresponding to a complete cycle in one year) is $1\,\mathrm{y}^{-1}$. An inspection of figure 3.1 reveals that the extratropical areas tend to have this expected value (they are coloured in white). Deviations from this behaviour are characterised by a faster average frequency, and are concentrated in the tropical area and also in a southern ocean band. If we look at the histogram of figure 3.1, we can see that the most probable average frequency corresponds to that of one cycle per year, and we can also note that the distribution has a long tail in the higher frequency side, while it decreases sharply in the low frequency side (only very few sites have an average frequency that is slightly lower than $1\,\mathrm{y}^{-1}$). This lack of "slow frequency" sites can be understood as being due to solar forcing: even if the oscillation induced by solar forcing is small, it produces at least one cycle per year. In many regions, due to other climatic processes, the average frequency is higher. Thus, we detect two main types of dynamics: regular sites and faster sites. We are going to discuss them in more detail.

We begin by considering the regular sites. We have chosen a typical one and its behaviour is analysed in figure 3.3. In addition to the annual solar forcing that produces the base of the regular trajectory, SAT dynamics has oscillations with shorter characteristic times, due to climatic processes like synoptic weather variability, which cause noisy deviations from the regular cycle. In this case, we note that the secondary oscillations have a significantly smaller amplitude than the annual cycle. If we look at the trajectory, we can see that the secondary cycles are not large enough to circle around the origin. Thus, even if they affect the instantaneous value of the frequency, they have a small effect on the average value. Therefore, in this site, the trajectory describes a well defined (but noisy) limit cycle, and we refer to this geographical site as a "regular site".

Next, we analyse geographical sites which have higher values of average frequency (examples are shown in figures 3.4 and 3.5). It is well-known that in tropical regions the annual solar forcing has a small amplitude, which is comparable to or even smaller than the amplitude of the oscillations induced by other (faster) climatic processes. Due to these additional oscillations, the Hilbert algorithm detects more than one oscillation per year, which results in the high value of frequency that we see in the red regions in figure 3.1. We

note that the average frequency does not correspond to a semi-annual cycle, as could be expected due to the characteristic solar forcing of the tropics (double crossing of the sun across the equator). We can understand the faster frequency by analysing the noisy trajectories: the cycles produced by the faster processes dominate the trajectory and can wash out the effect of the small-amplitude solar forcing (annual or semi-annual). Since many of these fast oscillations are wide enough to circle around the origin, they are counted as complete cycles and affect the frequency, increasing its average value and creating large fluctuations.

To yield light into the climate processes that can be represented in these fluctuations, let us consider the maps shown in figure 3.2: the standard deviation of frequency and the annual mean precipitation. While there are some differences in the extratropics, we observe a strong similarity between the two maps in the tropical regions. This is consistent with the fact that convective activity generates deep clouds that, on one hand, shield the surface from the solar radiation and can induce fast changes in the surface air temperature and, on the other hand, are responsible for the high level of precipitation. As for the extratropical region of high standard deviation located in the southern ocean, this region is characterised by large sea surface temperature (SST) gradients (fronts) and high eddy activity, which can strongly affect the above air temperature and can explain the strong fluctuations of instantaneous frequency.

In figure 3.6 we can see the results when frequency is calculated by using the linear trend of Hilbert phase, a procedure that washes out the frequency fluctuations that are due to "phase noise". The spatial patterns found in the map of time-averaged frequency and in the map of standard deviation of frequency are robust, in the sense that they are also found when frequency is computed with this other procedure. In contrast, the histograms of instantaneous frequency (figure 3.7) strongly depend on the procedure used to compute the frequency. In fact, this new procedure of frequency calculation washes out the phase oscillations that were producing the negative values of instantaneous frequency. To extract additional information from Hilbert frequency and to understand more deeply the meaning of its irregularities, we need to go beyond the analysis of the average and of the standard deviation. We need to apply more sophisticated approaches, such as the ones discussed in [85].

Now let us consider frequency and its fluctuations in the different seasons. Comparing the summer and winter maps shown in figure 3.8, we can see that in the tropics there are no large summer-winter differences (the average value of frequency and its standard deviation tend to be the same), but in the extratropics both the average frequency and its standard deviation tend to be higher in winter than in summer.

In particular, in the southern latitudes next to Antarctica, the average frequency is higher than $1\,\mathrm{y}^{-1}$ in winter and lower than $1\,\mathrm{y}^{-1}$ in summer. This is likely due to the existence of sea ice during winter that isolates the atmosphere from the ocean (acting as a buffer for air-sea interaction), thus allowing faster SAT fluctuations. In the midlatitude oceans, the air-sea contrast is larger in winter than in summer, and SST gradients are larger. Moreover, in winter the atmosphere is more active, thus allowing faster changes in SAT fluctuations and more day-to-day variability. In the tropics, SST is high during summer, particularly off the equator, and this is able to induce stronger convection leading to higher frequency in air temperature variability. Over continental areas, northern India presents the region with the smallest average frequency during summer, with a value lower than the annual cycle. This is likely related to the development of the convection associated with the Indian monsoon, which induces maximum rainfall amounts over that region. However, it is unclear why convection would diminish the average frequency instead of increasing it, as is the case over the tropical oceans. Further understanding is left for future studies.

3.6 Conclusions

We have calculated Hilbert instantaneous frequency from daily SAT series of the ERA-Interim dataset. As a first step, we found that the maps of average frequency uncover well defined large-scale patterns. In the extra-tropics, the average frequency generally corresponds to the expected one-year period of solar forcing, while the tropics generally display a faster behaviour. The results were interpreted as being due to the fact that in the tropics the amplitude of the annual oscillation is small in comparison to oscillations induced by other climatic processes. Coherent structures were also found in the maps of the standard deviation of frequency, which tend to be located over regions of strong annual precipitation. The main differences between summer and winter frequency behaviour were found in the extra-tropics, where the average frequency and the standard deviation tend to be higher during winters.

In general, the time series of instantaneous frequency display large fluctuations, whether the geographical site is a "regular" site with average frequency corresponding to one cycle per year, or an "irregular" site that displays a faster frequency dynamics. Such frequency fluctuations are often considered artifacts that can be removed by appropriated filtering. However, in the case of the SAT daily data analysed here, the frequency fluctuations indeed contain meaningful

information about large-scale climate phenomena.

Our results indicate that Hilbert analysis can be a valuable tool to gain information about the dynamics of climatic variables. In particular, it allows us to find patterns of different dynamics at a global scale, which are tied to different climatic conditions.

Chapter 4

Changes in SAT dynamics over the last 35 years

The results presented in the previous chapter motivated us to use the Hilbert time series of amplitude, $A(t)$, and frequency, $\omega(t)$, to quantify SAT changes. While changes in the SAT annual cycle have been investigated (a trend to reduced cycle amplitude has been detected in many regions [52–58]), changes in SAT dynamics over several decades have not been investigated yet at a global scale, to the best of our knowledge. In order to fill this gap, we use Hilbert analysis to investigate SAT time series with daily resolution. Our goal is to detect the regions where changes in SAT dynamics over the last 35 years are more pronounced. Specifically, we are interested in addressing the following questions: Which properties of $A(t)$ and $\omega(t)$ display relevant changes? In which regions are these changes more pronounced? Which processes can be responsible of these changes? Can these changes be used as a quantitative measure of regional climate change?

In section 4.1 we explain how we quantify changes in time series and how we evaluate the statistical significance of such changes. Then, in section 4.2 we present the results about amplitude change: maps of the relative changes of amplitude average and its variance. Analogously, in section 4.3 we present the results about frequency change. We also compare the results with a non-Hilbert approach. In section 4.4 we draw the conclusions of this work. Additionally, in section 4.5, we provide supporting results that show the robustness of our findings.

The results that we present in this chapter were published in [93].

4.1 Quantifying changes in SAT dynamics

4.1.1 Relative change

We quantify the relative change in Hilbert amplitude by

$$\frac{\Delta\overline{A}}{\overline{A}} = \frac{\overline{A}_\mathrm{l} - \overline{A}_\mathrm{f}}{\overline{A}}, \tag{4.1}$$

where $\overline{A}_\mathrm{f}$ is the time-averaged value of the amplitude during the first 10 years of the time series (1981–1990), and $\overline{A}_\mathrm{l}$ during the last 10 years (2006–2015). The simple notation $\overline{A}$ indicates the amplitude averaged over all the time series. Analogously, we calculate the relative change of amplitude variance, $\Delta\sigma_A^2/\sigma_A^2$, of frequency average, $\Delta\overline{\omega}/\overline{\omega}$, and of frequency variance, $\Delta\sigma_\omega^2/\sigma_\omega^2$. In section 4.5.2 we analyse how the uncovered spatial structures depend on the time intervals that we use to calculate the relative changes. While the values of the relative changes vary with the considered time interval, the spatial maps are remarkably robust as the same structures are found with the three time intervals considered.

We perform a similar analysis to detect changes by a non-Hilbert approach. Starting from the raw SAT time series, we compute the amplitude of the climatology and the variance of the anomaly time series. Specifically, the amplitude of the climatology time series $c(t)$ in the time interval I is calculated as

$$A^{(\mathrm{clim})}(I) = \max_t[c^I(t)] - \min_t[c^I(t)], \tag{4.2}$$

where $c^I(t)$ is the climatology series calculated only in the time interval I. We remark that the climatology amplitude $A^{(\mathrm{clim})}(I)$ is a scalar number that depends on the choice of the time interval I. We calculate the climatology amplitude in the first and last decade, as well as in the whole series. As before, we use these values to calculate the relative change, $\Delta A^{(\mathrm{clim})}/A^{(\mathrm{clim})}$. Also, the variance of the anomaly time series $z(t)$ is calculated and then used to find the relative change, $\Delta\sigma_z^2/\sigma_z^2$.

With the goal of relating changes in Hilbert frequency with changes in statistical properties of SAT time series, we perform an analysis of the number of zero-crossings: for each preprocessed SAT time series $x(t)$, we count the number of crossings through the mean value, $x = 0$. As with other quantities, we then calculate the relative change.

4.1.2 Significance analysis

A statistical significance analysis is performed by surrogating Hilbert series. For each amplitude time series (i.e. in each geographical site) we generate 100 shuffle surrogates of the amplitude series and for each surrogate we calculate the relative change $\Delta\overline{A}/\overline{A}$. Then, we calculate the average over the 100 surrogates, $\left\langle \Delta\overline{A}/\overline{A} \right\rangle_s$, and its standard deviation, σ_s, and use them to define the significance threshold. The relative change computed from the original data is considered significant if it is higher than $\left\langle \Delta\overline{A}/\overline{A} \right\rangle_s + 2\sigma_s$ or lower than $\left\langle \Delta\overline{A}/\overline{A} \right\rangle_s - 2\sigma_s$. In the colour maps, regions where changes are not significant are displayed in white. We apply the same test to frequency changes and the other quantities, except for the climatology, for which a surrogate test is not applicable. In section 4.5.1 various thresholds are considered and, in addition, a non-parametric significance test is used. Here we present only the maps obtained with threshold $\pm 2\sigma_s$, because it is a compromise between uncovering the spatial regions where SAT changes are pronounced and disregarding the areas where the changes are small.

4.2 Amplitude changes

In figure 4.1, panels (a) and (b) display the time-averaged amplitude, respectively in the first and in the last 10 years. Panel (c) displays the relative change of Hilbert amplitude, $\Delta\overline{A}/\overline{A}$. Here we see an area of large increase (more than 50%), located in Amazonia (red spot marked by a triangle), and an area of large decrease (again, more than 50%), located in the Arctic (blue spot marked by a circle). The raw SAT time series in these regions are displayed in figure 4.2.

In both time series we clearly observe a change in the amplitude of the oscillations in the last 10 years in comparison with the first 10 years, having a visual confirmation of the changes detected by Hilbert amplitude. The red spot in Amazonia, whose SAT series shown in figure 4.2(a) has an increasing amplitude, can be interpreted in terms of changes in precipitation. In particular, the increase of Hilbert amplitude is linked to the decrease of precipitation and to the lengthening of the dry season (as reported in [94–96]). This is due to the fact that, when precipitation decreases, the fraction of solar radiation that is not used for evaporation is used to heat the ground, which in turns heats the surface air. This leads to higher extreme temperatures during the dry seasons, as can be observed in figure 4.2(a). Regarding the blue spot in the Arctic region, whose SAT series shown in figure 4.2(b) has a decreasing amplitude, it can be interpreted as due to the melting of sea ice. In fact, when ice is present at the surface of the sea, it acts as an insulator, preventing heat exchange between

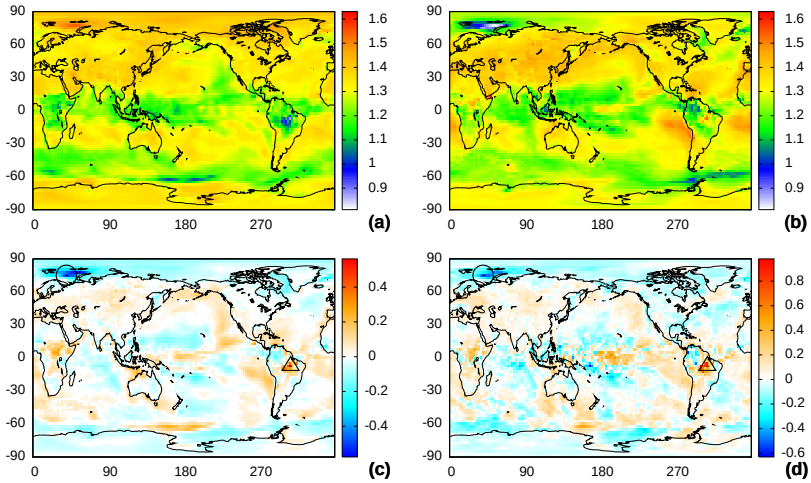

Figure 4.1: Relative change of time-averaged Hilbert amplitude. (**a**) Amplitude averaged over the first 10 years (1981–1990). (**b**) Amplitude averaged over the last 10 years (2006–2015). (**c**) Relative change of time-averaged Hilbert amplitude, $\Delta\overline{A}/\overline{A}$. (**d**) Relative change of the amplitude of the annual cycle, computed from the amplitude of the climatology, $\Delta A^{(\mathrm{clim})}/A^{(\mathrm{clim})}$. In (a) and (b), amplitude is represented in the same renormalised units as the preprocessed SAT series $x(t)$.

sea and air. This causes a large amplitude of SAT cycle. On the other hand, if the ice melts, the air-sea heat exchange reduces the amplitude of the cycle. In particular, during winter the air temperature is mitigated by the sea and tends to have more moderated values. It is important to take into account that this blue spot is in a region where the observational constraints from satellites on the reanalysis are scarce. This circumstance decreases the quality of the reanalysis in the region. Therefore, in order to check whether the detected changes are robust, we perform the same analysis using the NCEP-DOE reanalysis dataset. The results, presented in section 4.5.3, confirm the presence of the blue spot in the Arctic.

Next, we compare the changes detected by Hilbert amplitude with those computed by decomposing SAT time series into climatology and anomaly. Since the climatology term retains the annual cycle, we expect its amplitude change to give similar results as the Hilbert amplitude change. On the other hand, the anomaly term contains all the rapid variability, so we expect its variance to

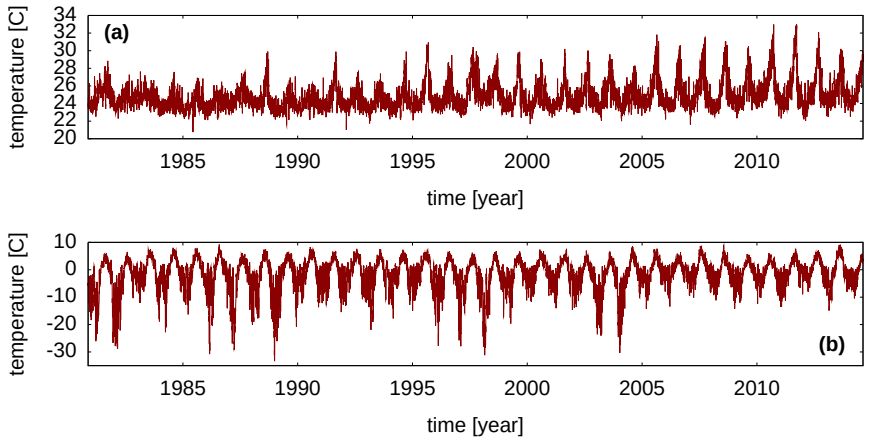

Figure 4.2: SAT time series in two regions where a clear change in the oscillation amplitude is found. (**a**) Site in Amazonia (7.5 S, 307.5 E), marked with a triangle in fig. 4.1(c). (**b**) Site in the Arctic (75 N, 40 E), marked with a circle in fig. 4.1(c).

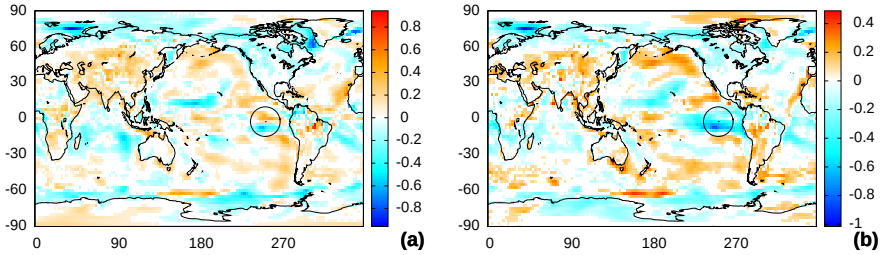

Figure 4.3: Relative change of amplitude fluctuations computed from the variance of (**a**) the Hilbert amplitude, $\Delta\sigma_A^2/\sigma_A^2$; (**b**) the anomaly time series, $\Delta\sigma_z^2/\sigma_z^2$.

give similar results as the variance of Hilbert amplitude.

Figures 4.1(c) and 4.1(d), which display respectively the relative change of time-averaged Hilbert amplitude and of climatology amplitude, and figures 4.3(a) and 4.3(b), which display respectively the relative change of Hilbert amplitude variance and of anomaly variance, confirm these expectations. A good qualitative agreement is seen in the spatial structures. Importantly, the structures uncovered

by time-averaged Hilbert amplitude are well-defined, in comparison with those uncovered by the analysis of the climatology amplitude, which look noisier. These results confirm that Hilbert analysis directly applied to unfiltered SAT indeed gives a physically meaningful instantaneous amplitude, with average and variance values that are consistent with those computed from SAT.

In figure 4.3, however, there is a difference in the eastern Pacific Ocean, in the area marked with a circle. In particular, in panel (b) there is an area with large decrease of variance (deep blue, around -100%), while in (a) the decrease is less pronounced (light blue, around -65%) and extended over a smaller area. In addition, in panel (a) there is an orange-red area that indicates a moderate increase of variance (around 45%), while in (b) such area is absent. The reasons underlying these differences will be discussed later.

4.3 Frequency changes

In figure 4.4, panel (a) displays the frequency averaged in the first 10 years, while panel (b) displays it in the last 10 years. Panel (c) displays the relative change, $\Delta\overline{\omega}/\overline{\omega}$. Here we note that in the eastern Pacific Ocean there are two small areas, enclosed by the circle, of intense increase (red) and decrease (blue) of frequency. They both represent frequency changes whose absolute values are larger than 100% and correspond to the same region where differences were detected in figure 4.3.

These two areas of opposite sign suggest that, between the initial and the final decade, there is a shift of the intertropical convergence zone (ITCZ) toward the north. The ITCZ involves strong convective activity, which causes rapid fluctuations of SAT, thus giving high values of instantaneous frequency, as shown in figure 4.4(a,b). Therefore, in the relative change of frequency, in regions corresponding to the initial position of the ITCZ we see a decrease, while in regions corresponding to the final position of the ITCZ we see an increase. For the same reason, the two red areas in the western Pacific Ocean (indicated by two squares) suggest an expansion of the tropical convective regions. This interpretation is in agreement with previous works that have related a northward shift of the ITCZ to an interhemispheric temperature gradient [97–101], as the one experienced during the last decades. Regarding the red areas in the north Atlantic, in the north Pacific and in the south Pacific, they are consistent with an increase in the occurrence of fronts which cause large daily fluctuations of temperature and thus an increase of Hilbert frequency.

To gain insight into the physical meaning of the changes that are captured by

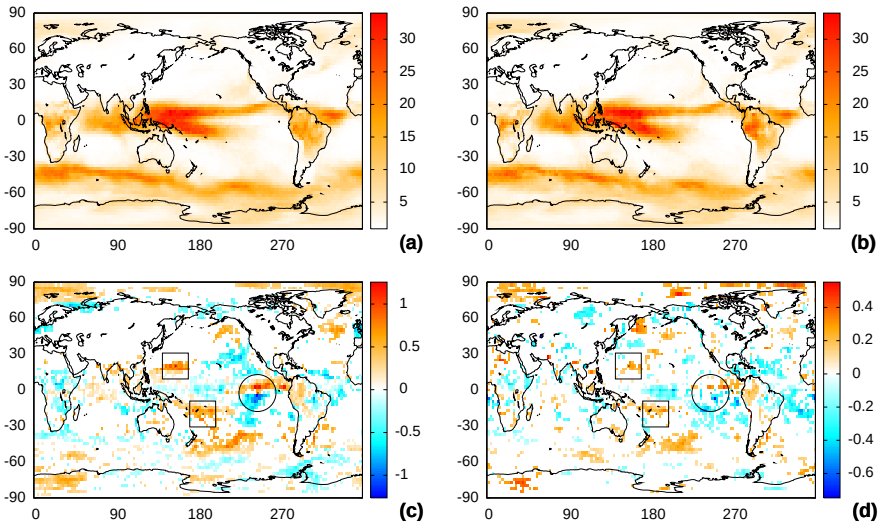

Figure 4.4: Relative change of time-averaged Hilbert frequency. (**a**) Frequency averaged in the first 10 years (1981–1990). (**b**) Frequency averaged in the last 10 years (2006–2015). (**c**) Relative change of Hilbert frequency, $\Delta\overline{\omega}/\overline{\omega}$. (**d**) Relative change of the number of zero-crossings of the normalised SAT time series. In (a) and (b), frequency is represented in units of y^{-1} and the colour scale is adjusted so that white represents a frequency value of $1\,\mathrm{y}^{-1}$.

Hilbert frequency, we use an alternative approach to estimate frequency changes: we define as "events" the zero crossings of SAT time series [69] (detrended and normalised to zero-mean, as described in section 2.4). Then, we count the number of events in the first 10 years, in the last 10 years, and calculate the relative change.

Figure 4.4(d) displays the map of relative change of zero-crossings. We see that there is a qualitative good agreement with the spatial structures seen in panel (c), thus providing a physical interpretation of the observed change of Hilbert frequency: the areas where the frequency increases (decreases) correspond to areas where the number of zero-crossings increases (decreases). We note that the relative changes in Hilbert frequency are more pronounced than those in the number of crossings, and this specifically holds in the regions where frequency changes are interpreted in terms of ITCZ migration.

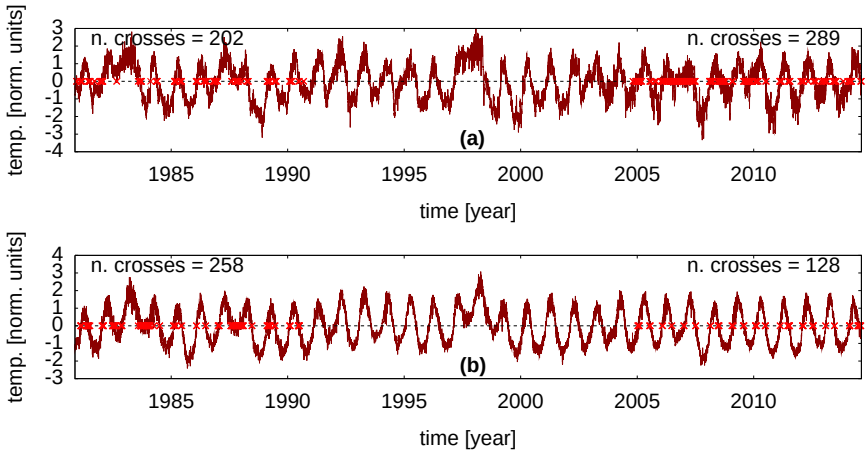

Figure 4.5: Normalised SAT time series and number of zero-crossings in the regions indicated with a circle in fig. 4.4(c). (**a**) In the red region (2.5 N, 245 E), the number of zero-crossings increases in the last 10 years in comparison with the first 10 years (from 202 to 289). (**b**) In the blue region (7.5 S, 250 E) it decreases (from 258 to 128).

Figure 4.5 displays the SAT time series in the dipole region indicated with the circle in figure 4.4(c), and also indicates the zero-crossings. We can understand the difference that was detected in this region between the variance of Hilbert amplitude and the variance of anomaly (fig. 4.3). This difference is explained in the following terms: in the first decade the seasonal cycle is more irregular than in the last decade, probably as a consequence of an El Niño event in 1982–1983. The anomaly series contains these slow fluctuations as well as the rapid ones, and thus its variance is affected by both effects. In contrast, the Hilbert amplitude is less affected by the slow fluctuations as its variance captures mainly the rapid fluctuations of SAT.

4.4 Conclusions

We have used Hilbert analysis to quantify the changes in SAT dynamics, in a global scale, that have occurred over 35 years. From the SAT time series with daily resolution we derived the amplitude and the frequency time series, and then calculated the relative change (between the first and the last decade) of average and variance of these series.

Large changes of Hilbert amplitude (more than 50%) in the Arctic and in Amazonia were interpreted respectively as due to ice melting and precipitation decrease. The analysis of Hilbert frequency also uncovered areas of large changes (more than 100%). In particular, two areas of opposite change in eastern Pacific Ocean and two areas of increase in western Pacific Ocean suggest a shift towards north and a widening of the ITCZ. While there is evidence that the ITCZ has moved north-south in the past, to the best of our knowledge our work is the first one to confirm this migration in the last decades. Our findings have important implications because, as the ITCZ is the ascending branch of the Hadley cell, its migration affects both the Earth's radiative balance and the release of latent heat that drives the tropical atmospheric circulation. Taken together, these effects have not only local but far-reaching climatic consequences. Additional analysis, provided in the appendices, confirms the robustness of these observations.

As the methodology used here can be applied to many other climatic time series that exhibit well defined oscillatory behaviour, we believe that our work will stimulate new research to identify and quantify the impacts of climate change.

4.5 Appendices

Here we provide additional analysis to support the results presented in this chapter.

In section 4.5.1 we discuss how the threshold used for the significance test affects the maps of relative changes. In addition, we apply a percentile-based significance test to confirm the validity of our results.

In section 4.5.2 we discuss how the obtained maps depend on the time intervals that we use to calculate the relative changes. Until now, we have used the first and final 10 years of the reanalysis to compute relative changes of time series. For comparison, here we use the first and final 5 years and also the first and final 17 years. Maps with very similar spatial structures are found, confirming the robustness of our findings.

Finally, in section 4.5.3, we compare the results obtained from the two reanalysis datasets (ERA-Interim and NCEP-DOE) and show that they uncover qualitatively similar spatial structures, for both amplitude and frequency. There are also some differences in the results, but they are due to relevant differences between the two reanalysis data.

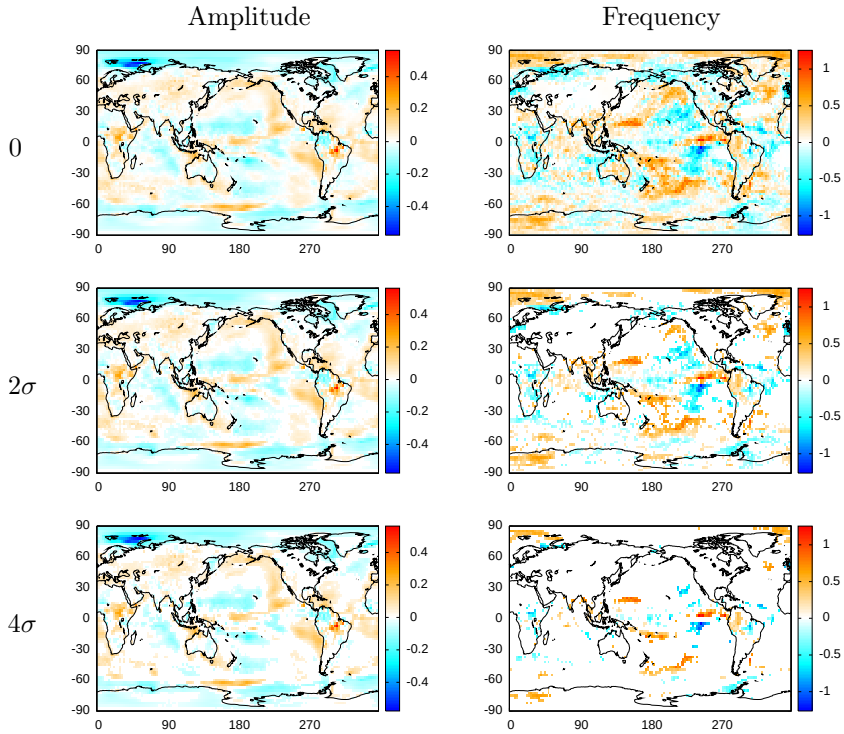

Figure 4.6: Maps of relative change of time-averaged amplitude (left column) and of time-averaged frequency (right column), with different values of the significance filter. First row: no filter. Second row: only values with a distance of at least 2σ from the average of the 100 surrogate values. Third row: as the second one, but with a threshold of 4σ.

4.5.1 Significance test

As we explained in section 4.1, we performed a significance test on the maps of relative change of the calculated quantities. We calculated 100 surrogate values of the same relative change, and from this ensemble we calculated the average μ and the standard deviation σ. Then, we considered the actual (no surrogate) relative change as statistically significant if its distance from μ is at least 2σ.

To see in more details how this technique works, in figure 4.6 we show examples of the maps of change of amplitude and frequency with different

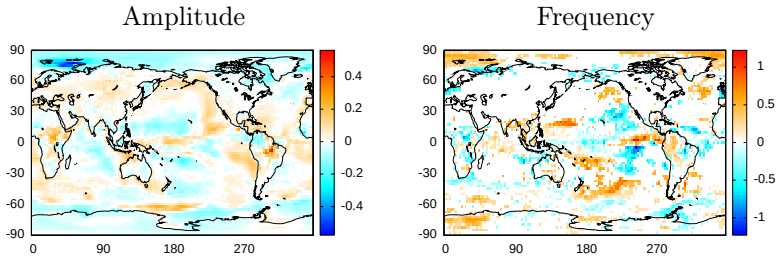

Figure 4.7: Maps of relative change of time-averaged amplitude (left) and of time-averaged frequency (right), obtained with the 95% percentile-based significance filter, computed with 100 surrogates.

choices of the threshold value. As expected, we see that the higher the threshold is, the more sites get erased from the map. Nonetheless, the main structures are still present even at 4σ, so we can conclude that they are robust with respect to the significance filtering.

An alternative significance test is based on the *percentile* of the values obtained from surrogated series. For example, we can consider a result (i.e. a relative change value) as statistically significant if it lies out of the range of the 95% central surrogate results. In figure 4.7 we present the maps of relative change of time-averaged amplitude (left) and of time-averaged frequency (right) obtained by using this criterion. A comparison with the two maps in figure 4.6 for threshold 2σ confirms that very similar spatial patterns are uncovered.

4.5.2 Influence of the time interval length

Here we analyse how the maps of relative change depend on the time period that we consider to calculate them. In the previous sections we used the first and final 10 years of the reanalysis (1981–1990 and 2006–2015) to calculate the relative change. Here, for comparison, we use the first and final 5 years (1981–1985 and 2011–2015) and also the first and final 17 years (1981–1997 and 1999–2015).

The results are shown in figure 4.8. The two columns display the changes of amplitude average (left) and frequency average (right). The different rows display results for various lengths of the time interval. We can see that, in the amplitude maps, the structures are robust and, in particular, the blue spot in the Arctic and the red spot in the Amazonia are present in the three maps. In

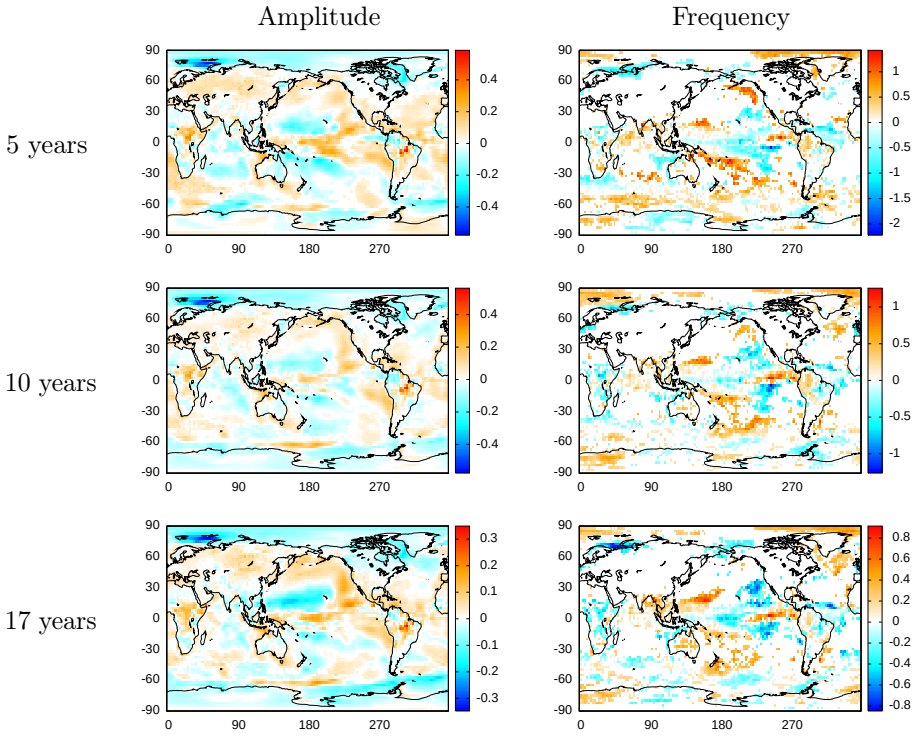

Figure 4.8: Relative change of time-averaged amplitude (left column) and of time-averaged frequency (right column). The relative change is calculated between the first and the last 5 years (first row), 10 years (second row), 17 years (third row).

the frequency maps, the dipole in the east Pacific Ocean and the red areas in the west Pacific Ocean are also present for all the interval lengths. While the spatial structures are very robust with respect to the considered time interval, the magnitude of the relative changes depends on the time interval. As could be expected, the changes are smaller when they are computed using longer intervals (third row).

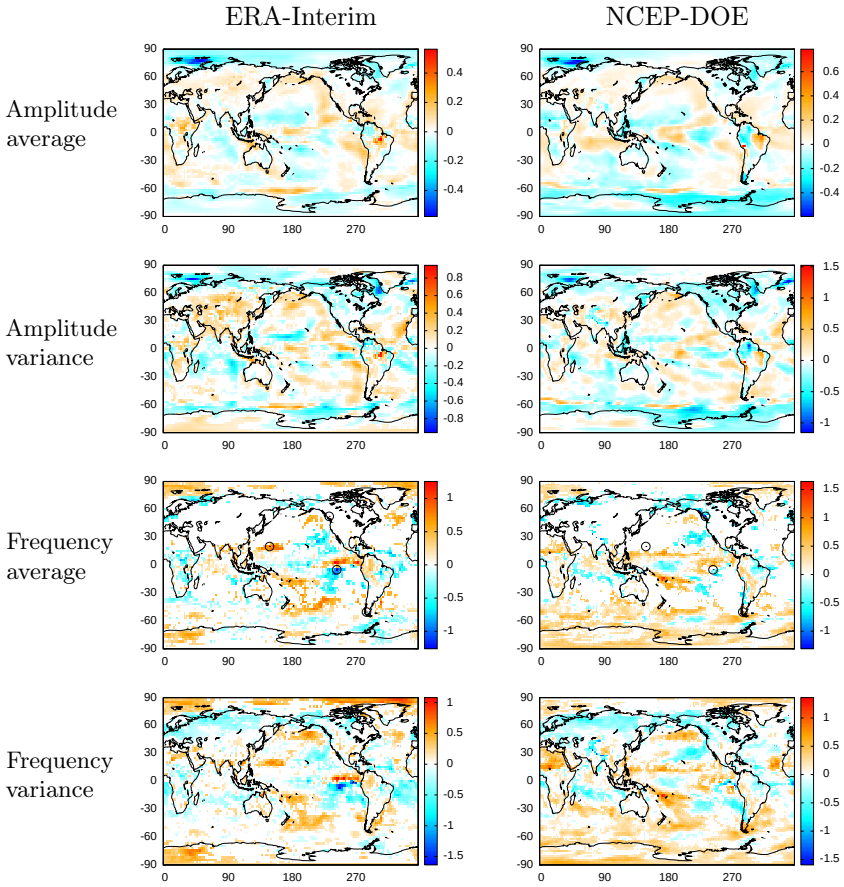

Figure 4.9: Comparison of results obtained from ERA-Interim (left column) and NCEP-DOE (right column). Relative change of amplitude average (first row), amplitude variance (second row), frequency average (third row), frequency variance (fourth row).

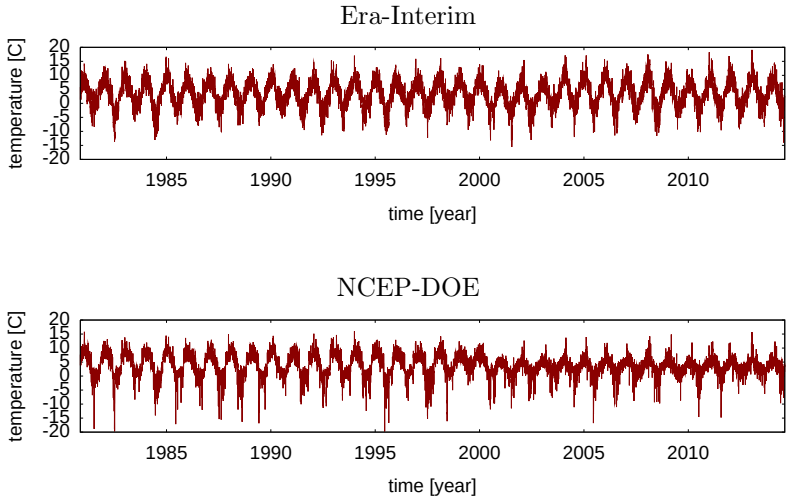

Figure 4.10: Comparison between SAT series of the same site (50 S, 287.5 E) in the two datasets: ERA-Interim and NCEP-DOE. This site is located in South America, indicated with a circle in figure 4.9 (third row).

4.5.3 Comparison with NCEP-DOE dataset

To test the robustness of our findings, in figure 4.9 we compare the maps of relative change of amplitude and frequency, obtained from two daily reanalysis datasets: ERA-Interim and NCEP-DOE AMIP-II Reanalysis.

In the first row we present the maps of change of amplitude average, while in the second row we present the maps of change of amplitude variance. A qualitative good agreement of spatial structures is seen. However, some differences can be noticed, such as in the Indian Ocean, where NCEP-DOE reanalysis gives an increase of amplitude average, while ERA gives a decrease. The third and fourth rows present the maps of change of frequency average and of frequency variance. Here again we can see a qualitative agreement, but there are also some relevant differences.

To investigate the reasons underlying these differences, we select in the maps of frequency average (fig. 4.9) some sites where the differences between the two maps are more pronounced. For example, in the same site one map shows a small change while the other one shows a large change. We find that there are indeed significant differences between the two SAT time series of the same site.

As an example, figure 4.10 displays the two SAT series in the site that is marked in South America. We see that the time series from ERA-Interim dataset maintains the same general trend throughout the entire length. On the other hand, the NCEP-DOE time series has a sudden change around year 2000, when the annual oscillation becomes significantly smaller and the rapid fluctuations get a more dominant role on the series. Therefore, Hilbert frequency is sensitive to this change and detects this difference between the two datasets, which is likely due to different models used to perform the reanalysis.

Therefore, Hilbert analysis is a useful data analysis tool to perform inter-model comparisons, because it captures temporal variations of amplitude and frequency that may not be detected by other analysis tools. It is an open question which reanalysis more closely represents the real SAT values.

Chapter 5

Unveiling temporal regularities in SAT

Uncovering meaningful regularities in complex oscillatory signals is a challenging problem with applications across a wide range of disciplines. In this chapter we present a novel approach, based on the Hilbert transform, and apply it to SAT time series.

In section 5.1 we show that temporal periodicity can be uncovered by smoothing the SAT series in a moving window of appropriated length τ before applying the HT. By analysing the dependence of the mean rotation period, $\overline{T}$, of the Hilbert phase on τ, we discover well-defined plateaus, that reveal the presence of stochastic periodicity in SAT dynamics. In many geographical regions the plateaus correspond to the expected one-year solar cycle. However, in regions where SAT dynamics is highly irregular, the plateaus reveal non-trivial periodicities, which can be interpreted in terms of climatic phenomena such as El Niño.

To gain further insight, in section 5.2 we study how the instantaneous Hilbert phase $\varphi(t)$ depends on the date of the year, for various values of τ. For τ within a plateau, the plot of $\varphi(t)$ vs. date unveils temporal structures, which provide a qualitative way to evaluate differences in SAT dynamics in different regions.

In section 5.3 we analyse how the obtained results reflect different climatic regimes. We discuss, as particular examples, the results in six geographical regions, which we refer to as regular ($\overline{T} = 1$ year, regardless of τ), quasi-regular ($\overline{T}$ reaches a one year plateau, for τ large enough), double period ($\overline{T} \approx$ half year in a range of values of τ), irregular (in the plot of $\overline{T}$ vs. τ no plateau is found),

El Niño ($\overline{T}$ vs. τ displays a plateau at $\overline{T} \approx 4$ years, which is consistent with the El Niño phenomenon) and QBO (a plateau is found at $\overline{T} \approx 2.5$ years, which is consistent with the Quasi-Biennial Oscillation).

In section 5.4, the dependence of $\overline{T}$ on τ is given to a standard machine learning algorithm, to classify the gridded sites of the dataset into distinct geographical regions. The results demonstrate that the dependence of $\overline{T}$ indeed reveals meaningful information and constitutes a new approach for SAT time series classification.

In section 5.5 we draw our conclusions. The results demonstrate that Hilbert analysis, combined with temporal averaging, is a powerful new tool that can uncover hidden temporal regularity in complex oscillatory signals.

In section 5.6 we give additional evidence to support the validity of our results. We compare our approach with Fourier analysis and find that the latter is not always able to detect periodicities in SAT dynamics. We also analyse synthetic time series generated with a simple model and confirm that our method extracts information that is fully consistent with our knowledge of the model that generates the data. Remarkably, the dependence of $\overline{T}$ on τ in the synthetic data is similar to that observed in real SAT data. Finally, we compare the results given by different datasets and find that they are consistent.

The results that we present in this chapter were submitted for publication. A preprint is available at [102].

5.1 Dependence of the mean period on the smoothing length

As we explained in section 2.4, we start from the raw SAT time series, $r_j(t)$, and we smooth it by a moving temporal average over a window of length τ. After the smoothing, we apply the HT and unwrap the phase time series, $\varphi_j(t)$. Then, we calculate the mean rotation period of the Hilbert phase as

$$\overline{T}_j = 2\pi \frac{\Delta t}{\Delta \varphi_j} \tag{5.1}$$

where Δt is the time interval between the first and the last day of the time series (in units of years) and $\Delta\varphi_j$ (in radians) is the variation of the unwrapped phase during this time interval.

We begin by analysing how $\overline{T}$ varies with τ. We consider odd values of τ between 1 day (no smoothing) and 149 days. We limit the length to this range in order to avoid filtering out the annual cycle.

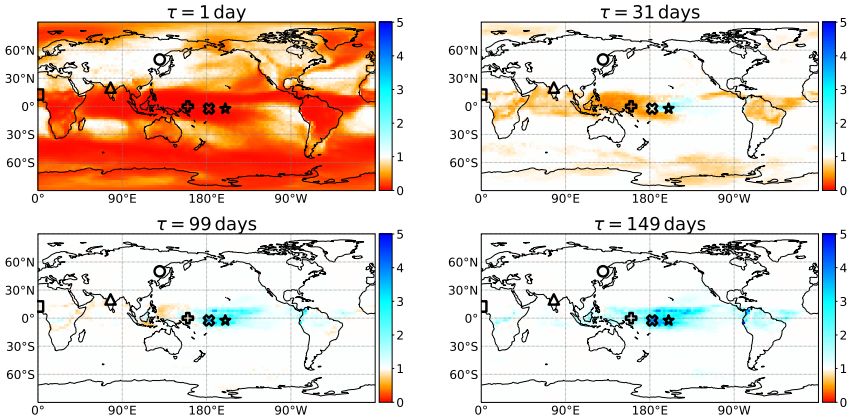

Figure 5.1: Influence of the smoothing on the mean rotation period. The colour maps display $\overline{T}$ (measured in years) computed after smoothing SAT by averaging in a moving window of length $\tau = 1$ (no smoothing), 31, 99 and 149 days. The symbols indicate the geographical sites discussed in the text: regular (circle), quasi-regular (triangle), double period (square), irregular (plus), El Niño (cross), QBO (star). At `https://youtu.be/5oX5i5uCm_8` a video shows the evolution of $\overline{T}$ as τ increases from 1 to 149 days.

Figure 5.1 displays the colour maps of $\overline{T}$, obtained with $\tau = 1$, 31, 99 and 149 days. White colour indicates a mean period of 1 year; red colour represents faster dynamics, while blue colour represents slower dynamics. As one could expect, as τ is increased the regions of fast dynamics are washed out. With $\tau = 31$ days, a blue area of slow dynamics begins to emerge in the central Pacific Ocean. This is due to the fact that in this area large-scale variability modes (such as El Niño) produce temperature oscillations with time scale of several years and whose amplitude is larger than the annual oscillation.

In order to gain insight into how the slow dynamics emerges, we focus the analysis on six geographical sites that are representative of different types of SAT dynamics. The symbols in figure 5.1 indicate the position of the six sites, which will be referred to as: regular, quasi-regular, double period, irregular, El Niño, and QBO.

Figure 5.2 displays, for the six sites, the dependence of $\overline{T}$ on τ. We can see that, except for the irregular site, in the other sites $\overline{T}$ shows a plateau in some range of values of τ. For the regular, quasi-regular and double period sites the

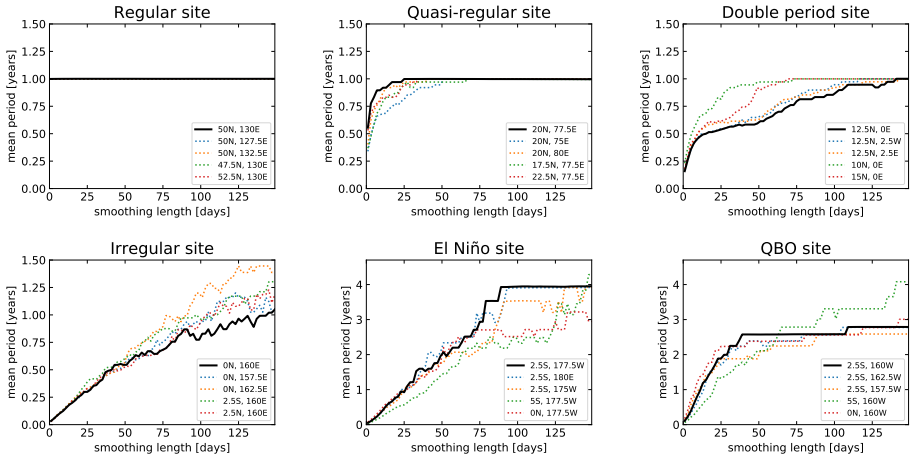

Figure 5.2: Dependence of the mean period $\overline{T}$ on the length τ of the smoothing window. The solid line represents the studied site, while the dashed lines represent the four neighbouring sites.

plateau is at $\overline{T} = 1$ year. The double period site shows also an irregular plateau at $\overline{T} \approx 0.5$ years. For the El Niño and QBO sites, the plateau is at $\overline{T} \approx 4$ years and $\overline{T} \approx 2.5$ years, respectively.

5.2 Relation between phase and date of the year

In order to demonstrate that plateaus uncover underlying regularities in SAT dynamics, we represent for each site the scatter plot of SAT vs. date of the year and Hilbert phase vs. date of the year, without pre-smoothing (fig. 5.3) and with pre-smoothing (fig. 5.4), using values of τ that are in the plateau in each site (in the irregular site there is no plateau and we just choose for τ the same value as in the other Pacific sites).

In figure 5.3 the width of the SAT curves is a measure of the interannual variability in each location (note the different vertical scales of the SAT panels). We can observe that the continental extratropical site (the regular one) has larger interannual variability than the two continental tropical sites (quasi-regular and double period), which in turn have larger interannual variability than the three oceanic tropical sites (irregular, El Niño, and QBO). This is

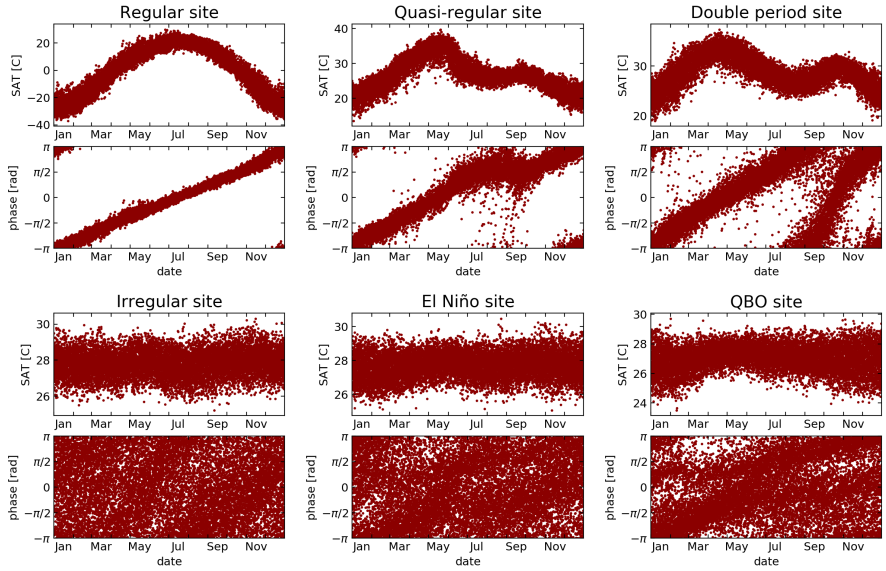

Figure 5.3: Hilbert analysis applied to SAT series without the initial smoothing. For each site the scatter plots display SAT vs. date of the year (upper panel) and Hilbert phase vs. date of the year (lower panel).

consistent with current understanding of atmospheric variability. Regarding the seasonal variations, the continental sites show well defined dependences with one or two maxima that are well captured in the phase scatter plots. On the contrary, the oceanic tropical sites show a weak or null seasonal cycle. The two easternmost sites show an interannual variability that is maximum during boreal winter and minimum during boreal spring. In figure 5.4 we see that clear structures emerge in the scatter plots of SAT vs. date and phase vs. date, when smoothing the raw SAT using a window of specific length τ.

5.3 Analysis of SAT dynamics

Taken together, figures 5.2, 5.3 and 5.4 allow us to uncover temporal regularities and to characterise SAT dynamics in each of the six sites.

In the regular site, we see in figure 5.2 that $\overline{T}$ as a function of τ is remarkably constant. The relation between phase and date of the year, even for the raw

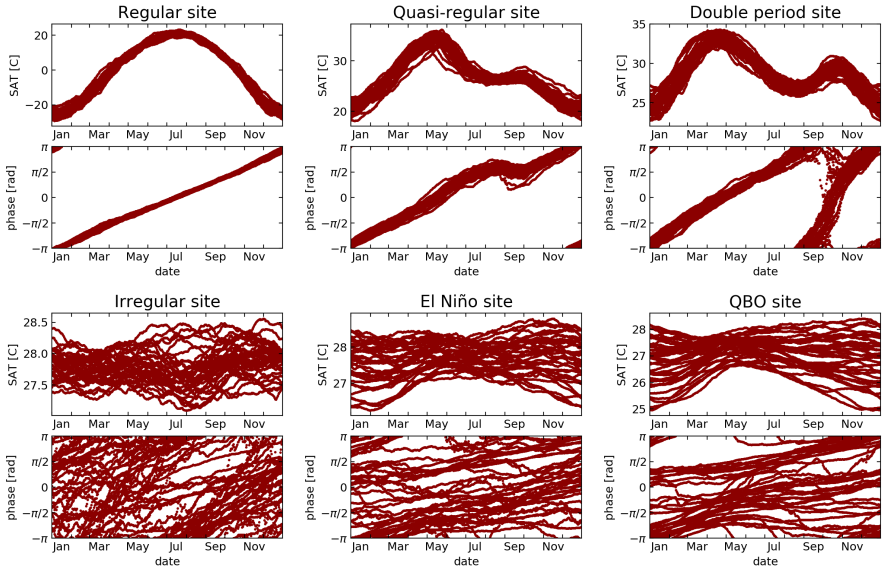

Figure 5.4: Hilbert analysis applied to smoothed SAT series. As in figure 5.3, but using a smoothing window with length τ in the plateaus shown in figure 5.2: $\tau = 41$ days for regular, quasi-regular and double period sites; and $\tau = 101$ days for irregular, El Niño and QBO sites.

SAT (fig. 5.3), is a clear linear growth that gives one cycle per year, and we see in figure 5.4 that smoothing the initial SAT series doesn't change this linear behaviour. This is due to the fact that in this site the dominating mode of SAT oscillation is produced by solar forcing, which in this region has a period of one year. The phase dynamics of the regular site is characteristic of continental extratropical climate, dominated by the annual cycle of solar forcing.

In the quasi-regular site, located in India, we see in figure 5.2 that without smoothing we get $\overline{T} \approx 0.5$ years. As τ increases, $\overline{T}$ increases until it reaches a stable plateau of $\overline{T} = 1$ year at $\tau = 25$ days. In the phase-date relation obtained without smoothing, we see that the phase has additional cycles during the year: there are years with just one cycle, and years with two or more cycles. If the smoothing window is long enough (in fig. 5.4 we used $\tau = 41$ days), these additional cycles are washed out, resulting in a phase-date relation with one cycle per year. We interpret these results as due to the fact that SAT in this

site has a component with year periodicity, and also half-year periodicity and faster variability, which are reduced by the 41-day smoothing that leaves the time series dominated by the annual cycle. We note in figure 5.4 that the phase increase is not linear during June-September, a result that captures the effect of the Indian monsoon that produces the small plateau in temperature in the same months.

The double period site is located in another monsoon region, in this case the West African monsoon. The plot of the mean period starts, for no smoothing, with $\overline{T} \approx 0.2$ years. As τ increases, $\overline{T}$ has a steep increase until $\tau \approx 10$ days, then it shows a slower growth for τ in the range of 10–45 days, with a mean period of $\overline{T} \approx 0.5$ years. When τ is increased further, $\overline{T}$ continues to grow reaching the one year period at $\tau \approx 140$ days. We interpret this behaviour as due to the presence of a component of half-year period whose amplitude is larger than the component with one year periodicity. In the SAT-date and phase-date scatter plots, with no smoothing (fig. 5.3) we see a noisy double cycle, while with 41-day smoothing (fig. 5.4) we are left with a dominant half-year oscillatory component. If we increase τ, we gradually eliminate the half-yearly component and extract a one year periodicity (not shown). The stochastic half year period in this region captures the northward movement of the intertropical convergence zone during boreal summer, which strongly affects the surface temperature leading to peaks before and after the monsoon.

The irregular site is the westernmost of the three sites in the tropical Pacific Ocean. We see that, for no smoothing, $\overline{T}$ starts from a low value ($\overline{T} < 0.1$ years) and, as τ is increased, $\overline{T}$ increases without revealing any particular time scale, i.e. it does not reach any plateau. The phase-date relation with no smoothing does not reveal any structure in the temperature dynamics, although there is a hint of a double period seen as a relative increase in the density of points, as would be expected for a region on the equator. If we smooth with $\tau = 101$ days, we still get a phase-date plot that doesn't suggest any clear time scale. These results indicate that in this region there is no dominating component of any particular period, i.e. SAT time series is consistent with the sum of stochastic processes with different time scales and similar amplitudes.

Next, we analyse the El Niño site, the central of the three sites in Pacific Ocean, located in the so-called cold tongue region. As in the previous site, without smoothing we find that $\overline{T} < 0.1$ years and then $\overline{T}$ increases linearly with τ. However, in contrast to the irregular site, here $\overline{T}$ reaches a stable plateau of $\overline{T} \approx 4$ years at $\tau \approx 90$ days. This means that, if we smooth SAT using a sufficiently long temporal window, we are left with a dominant oscillation whose period is approximately 4 years. In the phase-date relation a 4-year cycle would

be represented by a line that cycles 4 times in the horizontal direction while covering vertically the 2π phase range. In the phase-date relation calculated with $\tau = 101$ days (fig. 5.4) we see a hint of such ordered phase dynamics (in the form of tilted regions with higher density of points), which is not seen in the phase-date relation computed from the raw data (fig. 5.3). This is interpreted as an effect of El Niño, which has a period between 3 and 7 years, and whose effects are maximum in the equatorial Pacific cold tongue region. We want to point out that, since El Niño does not have a regular cycle, we expect that we cannot see a clear sign of it in figure 5.4, which has annual time scale.

In the QBO site (the easternmost of the three Pacific sites) $\overline{T}$ starts with a steep increase from $\overline{T} \approx 0.1$ years, then at $\tau \approx 40$ days it reaches a plateau of $\overline{T} \approx 2.5$ years. We interpret here that Hilbert phase analysis captures the effects of the QBO oscillation, which consists in the alternation of zonal winds between easterlies and westerlies in the tropical stratosphere, with a mean period of 28–29 months, and which has been shown to influence SAT [24, 25]. In the phase-date relation calculated after smoothing SAT in a window of $\tau = 101$ days (fig. 5.4) we see two tilted bands with higher density of points (consistent with a noisy cycle with a period of 2.5 year), which are not so evident in the phase-date relation obtained from the raw SAT (fig. 5.3).

5.4 Classification of SAT dynamics

To further demonstrate that the analysis of the dependence of $\overline{T}$ on τ indeed extracts meaningful information, we use the method of k-means clustering to classify the sites into a given number of clusters. Specifically, for each site we take as features the values of $\overline{T}$ for $\tau = 1, 9, 29, 49, \ldots, 149$ days. Then, we use the k-means algorithm to classify the 10512 geographical sites into n clusters based on these features. In figures 5.5 and 5.6 we report the results for $n = 4$ (consistent results where obtained with larger n, the analysis is in progress and will be reported elsewhere). It is interesting to note that the map has similarities with the upper left panel of figure 5.1.

In particular, the blue cluster characterises regions dominated by the annual cycle and large temperature variations (see the regular site). These include the northern extratropical land masses and storm track regions over the Pacific and Atlantic oceans. In the southern hemisphere, this cluster characterises the extratropical continents and subtropical oceans, but most of the southern extratropics are in the orange cluster. This latter cluster characterises regions with faster dynamics that are dominated by the annual cycle only after smoothing

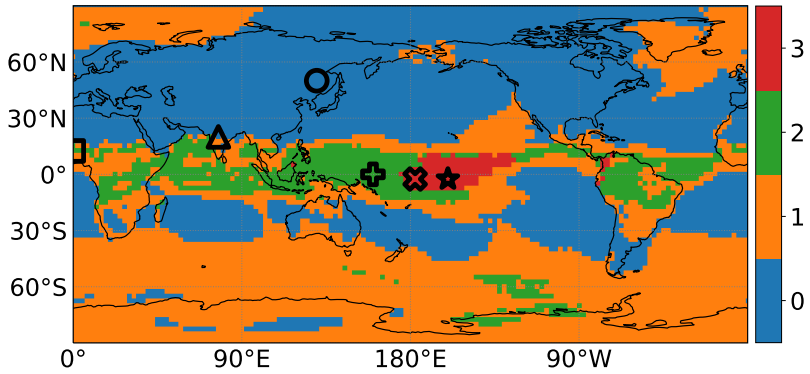

Figure 5.5: Classification of the geographical sites in four clusters. The k-means algorithm is used to classify the sites according to their values of $\overline{T}$ for different choices of τ. We indicate the six chosen sites as we do in fig. 5.1.

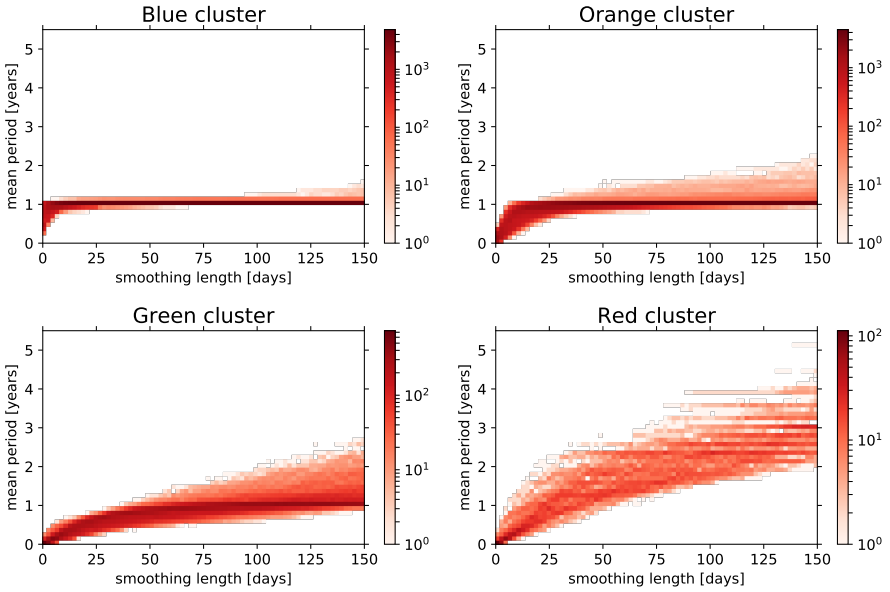

Figure 5.6: Dependence of $\overline{T}$ on τ in each cluster, represented as a 2D histogram. The colour code indicates the number of sites in each bin; white represents the empty bins.

with $\tau > 20$ days, which may reflect the importance of subseasonal variability in the southern hemisphere.

The tropical band is dominated by the green cluster, which is composed by regions of low temperature variability and whose spatial structure is closely related to the mean rainfall pattern. The green cluster characterises regions where no plateau is found when increasing the smoothing length. The largest green region (where the irregular site is located) is the western Pacific warm pool, which presents temperature variability that is strongly tied to convection on short time scales and thus shows up in this study as with irregular behaviour.

Finally, the red cluster characterises the central Pacific, the region that for $\tau > 30$ days has the slowest dynamics (as can be seen in fig. 5.1). Note that the core of the cold tongue region has a strong annual cycle and therefore it is within the blue cluster. The red cluster marks a transition region between the strong wind-driven equatorial cold tongue dynamics and the weak and thermodynamic-driven variability of the western Pacific warm pool. It is a region with relatively weak annual cycle and influenced by El Niño and the QBO and thus shows slow dynamics (see El Niño and QBO sites). The quasi-regular and double-period sites are located in cluster borders because they are monsoon regions and thus rainfall and temperature variations are strongly related during summertime, giving rise to large deviations from the annual cycle. Similar behaviour is expected in southeast Asia and central America and subtropical South America.

5.5 Conclusions

In summary, we have presented a novel method for extracting information from complex oscillatory signals. Studying SAT time series, we have shown that Hilbert phase analysis combined with temporal averaging allows to extract different oscillatory modes. The proposed method is based on the analysis of the dependence of the mean rotation period of the Hilbert phase, $\overline{T}$, on the length of the smoothing window, τ. We have discovered that $\overline{T}$ vs. τ exhibits well-defined plateaus, which reveal hidden regularities in SAT dynamics. In addition, this information, used in a machine learning algorithm, provides a novel way to classify different types of SAT dynamics.

Taken together, our results demonstrate that the method proposed here can be used for uncovering hidden temporal regularities and for the classification of different oscillatory behaviours. An advantage of our approach is that it allows continuous tuning of the time scale in which SAT variability is washed out.

5.6 Appendices

Here we provide additional analysis to support the results presented in this chapter.

In section 5.6.1 we compare the results of Hilbert analysis with those of Fourier analysis. We show that the plateau behaviour and the gradual variation of $\overline{T}$ are not necessarily detected by Fourier analysis because, as τ increases, the frequency of the dominant peak in the power spectrum is either constant or changes abruptly.

Then, in section 5.6.2 we generate synthetic SAT time series with a simple model to test and validate our analysis method. Applying our analysis method to these time series we get results in good agreement with our knowledge of the model that generates the data. Also, tuning the model, we can reproduce the same plot of $\overline{T}$ vs. τ as in four of the chosen sites.

In section 5.6.3 we compare the results given by the two datasets (ERA-Interim and NCEP-DOE). We find consistent results, while the only discrepancies are due to differences in the grid resolution.

Finally, in section 5.6.4 we calculate the mean period from a monthly SAT dataset and find results that are consistent with the ones obtained from smoothed daily data.

5.6.1 Fourier analysis

Here we investigate if Fourier spectral analysis can detect the temporal regularities detected by Hilbert phase analysis. To do this, we analyse how the highest peak, f, in the power spectrum depends on τ. Figure 5.7 shows the plot of $T = 1/f$ vs. τ. Only in the regular site we find the same dependence that we find with Hilbert analysis. In the other sites we get totally different results: the plateaus and the gradual dependence of T on τ are lost, because T is either constant or it changes abruptly.

In the regular and in the quasi-regular sites, Fourier gives a period equal to 1 year, regardless of τ, while we have seen in figure 5.2 that the quasi-regular site starts with a faster dynamics and then the period rapidly increases to the stable value of 1 year. In the double period site, the period starts at $T = 0.5$ years and remains constant as τ increases until $\tau = 25$ days, where it suddenly jumps to $T = 1$ year. Thus, here we lose the gradual variation captured with Hilbert analysis. In the irregular site, we have a similar sudden jump, from $T = 0.5$ years to $T \approx 1.3$ years at $\tau \approx 90$ days. In contrast, Hilbert analysis and the phase-date relation tell us that there is no dominating oscillatory component

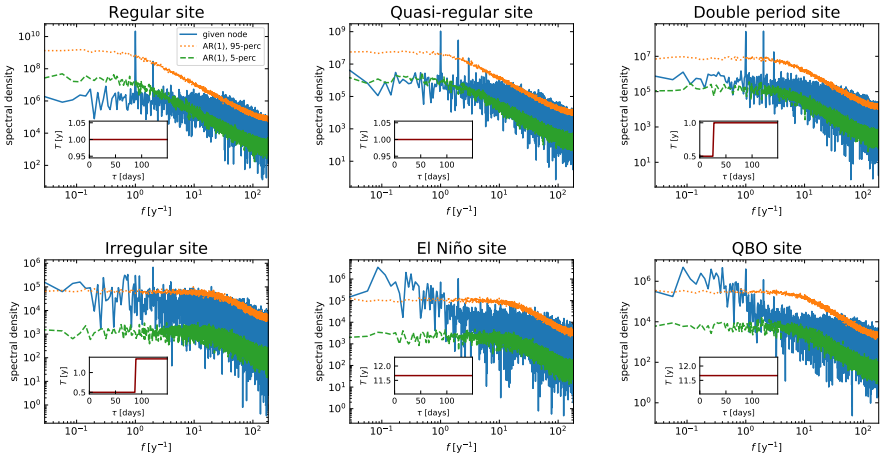

Figure 5.7: Fourier analysis of SAT time series. The panels display the power spectrum of the SAT time series in the different sites (without pre-smoothing, in blue). We test the statistical significance of the Fourier peaks with 100 realizations of AR(1) series with the same variance and autocorrelation (at lag 1) as the SAT series (the green and orange lines indicate the 5 and 95 percentiles, respectively). We analyse the influence of smoothing by computing the spectra after smoothing the SAT time series using a window of length τ. For each value of τ we calculate the dominant period, T, as the inverse of the frequency of the strongest significant peak in the spectrum. The insets show the dependence of T on τ.

at any smoothing length. In El Niño and QBO sites, $T \approx 11.7$ years, regardless of τ, which is due to the fact that the Pacific has variability from interannual to interdecadal time scales, and thus, SAT Fourier spectrum has high energy at low frequencies.

Thus, an advantage of our Hilbert approach, compared to Fourier analysis, is that it allows to detect the gradual emergence of temporal regularity.

5.6.2 Analysis of synthetic data

We further validate the proposed analysis method using synthetic data generated with a simple model. We demonstrate that Hilbert analysis returns information which is fully consistent with our knowledge of the equation that generates the data. In other words, the dependence of $\overline{T}$ on τ is as one would expect,

considering the parameters used to generate the synthetic time series. In addition to validating the analysis method, we also show that this model provides a simple way to understand the dependence of $\overline{T}$ on τ found in real SAT data. The model that we consider is the sum of two sinusoidal oscillations (the annual cycle and a slower oscillation) and autoregressive noise:

$$S(t) = \frac{a\sqrt{2}\cos(\omega_{\mathrm{sl}}t) + b\sqrt{2}\cos(\omega_{\mathrm{y}}t) + c\varepsilon(t)}{\sqrt{a^2+b^2+c^2}}, \tag{5.2}$$

where $\omega_{\mathrm{sl}} = \frac{1}{4}2\pi$ rad/year represents a slow 4-year cycle, $\omega_{\mathrm{y}} = 2\pi$ rad/year represents a 1-year cycle, and $\varepsilon(t)$ represents AR(1) noise with zero mean and unit variance and with persistence $\gamma \in [0,1]$. We use AR(1) because it is the usual null hypothesis to model climate data [103]. With this model, using a sampling time $\Delta t = 1$ day, we generate time series of the same length as ERA daily reanalysis (14245 days). The parameters a, b, c allow us to vary the amplitude of the three components, while the normalization factors ($\sqrt{2}$ and $\sqrt{a^2+b^2+c^2}$) keep constant the first and second moment of the distribution of $S(t)$ values (zero mean and unit variance). From the synthetic time series we calculate the mean period $\overline{T}$, following the same procedure as for the SAT reanalysis time series.

Figure 5.8 displays the dependence of $\overline{T}$ on τ and compares the results of real and synthetic data. We can see that the regular site is fitted by our model without slow cycle and with low noise ($a = 0, b = 6, c = 2$). The quasi-regular site is fitted when the noise is higher, but still lower than the one-year cycle ($a = 1, b = 10, c = 6$). The irregular site is fitted when the noise is higher that the one-year cycle ($a = 0, b = 2, c = 6$). On the other hand, the El Niño site is fitted when the slow cycle and the one-year cycle have comparable amplitudes, and the noise has even higher amplitude ($a = 5, b = 4, c = 9$).

Finally, in figure 5.9 we choose the parameter values that best fit the El Niño site and analyse how the mean period depends on the parameters and on the smoothing length τ. As we could expect, we see that increasing the parameter c (noise) decreases the mean period. This is because it increases the amplitude of high frequency oscillations, shortening the mean period. On the other hand, increasing a (b) increases the strength of the slow cycle (of the one one-year cycle), resulting in a longer mean period (in a mean period that is closer to one year).

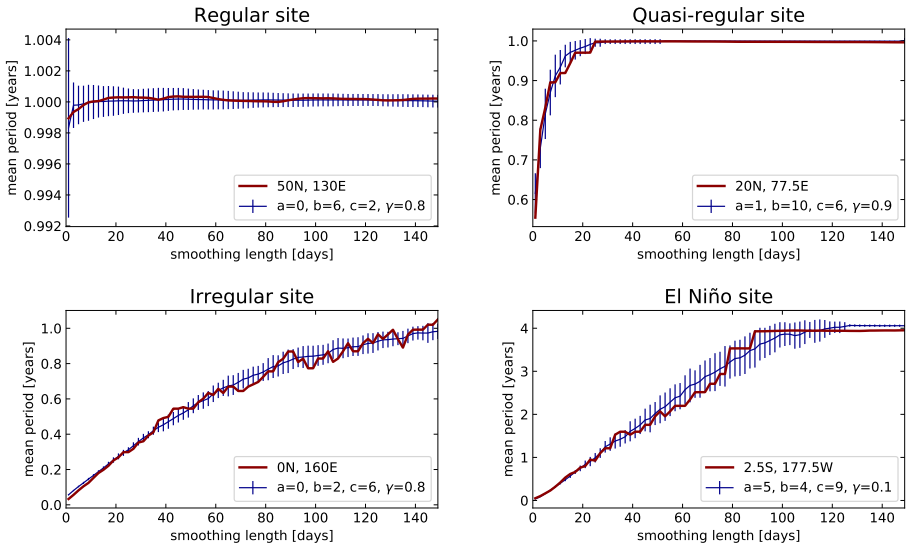

Figure 5.8: Dependence of the mean period $\overline{T}$ on the smoothing length τ. Red colour indicates results from the SAT series of an actual geographical site, while blue colour indicates results from 20 realizations of synthetic data (the error bars represent the standard deviations). For each of the four represented geographical sites, we search for the synthetic series that best fits the dependence of $\overline{T}$ on τ. To find it, we vary a, b, c from 0 to 10 with steps of 1, while γ varies from 0 to 0.9 with steps of 0.1. In the legend of each panel, we show the coordinates of the geographical site and the parameter values that best fit the period dependence.

5.6.3 Comparison with NCEP-DOE dataset

To demonstrate the robustness of our findings, here we compare the results obtained from ERA-Interim with those obtained from NCEP-DOE.

Figure 5.10 shows the dependence of $\overline{T}$ on τ for the six chosen geographical sites. Comparing with the results obtained from ERA-Interim (fig. 5.2), a good agreement is observed between the two reanalyses. There are some differences in the double period site and the El Niño site, that may be due to the fact that the two reanalysis datasets are not in the same spatial grid, and the gradients in behaviour can be very large. In other words, in this region small changes of position can give very different SAT dynamics.

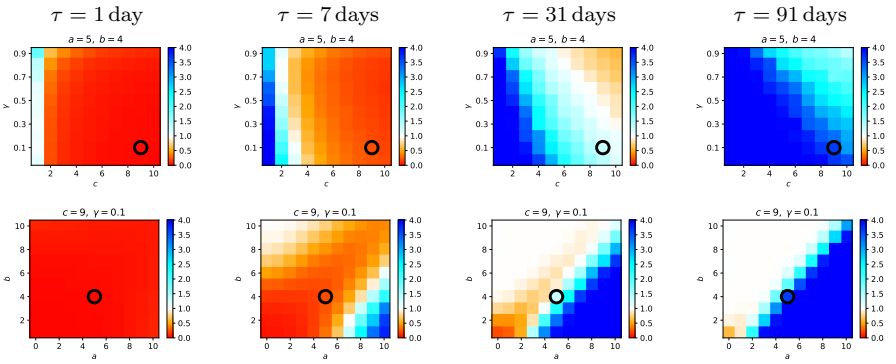

Figure 5.9: Colour plots representing the mean period (in years) obtained from the synthetic series that best fits the El Niño site. In the upper row we choose a and b to best fit the El Niño site, while in the lower row we choose c and γ to best fit that site. The cirlce indicates the values of the two free parameters that produce the best fit.

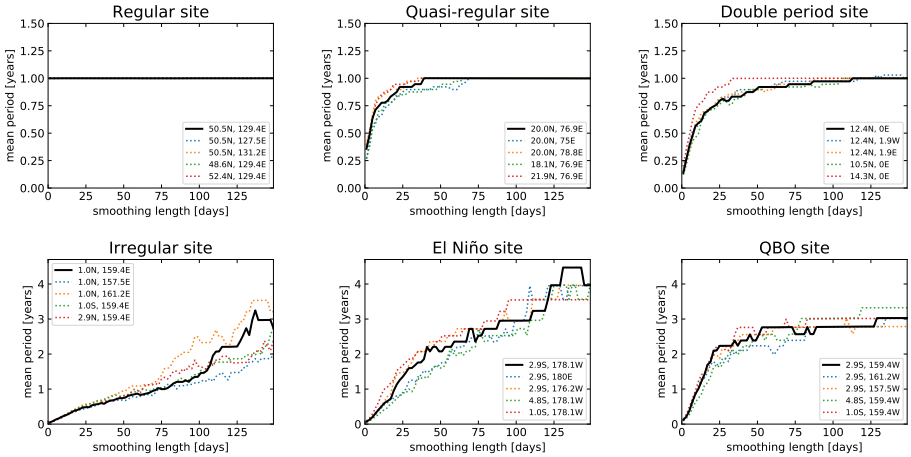

Figure 5.10: Dependence of the mean period $\overline{T}$ on the smoothing length τ, obtained from NCEP-DOE dataset.

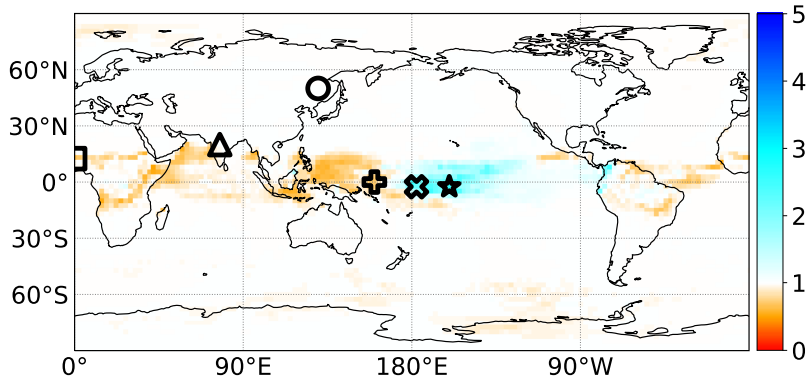

Figure 5.11: The colour map displays $\overline{T}$ (measured in years) computed from ERA-Interim with monthly time resolution and without smoothing.

5.6.4 Comparison with monthly SAT

Finally, by considering ERA-Interim reanalysis with monthly time resolution and without smoothing, we test the influence of time resolution. In figure 5.11 we can see that the mean period obtained with monthly resolution is consistent with the results presented in figure 5.1 and obtained with daily resolution. Specifically, we note that this map obtained from monthly SAT data looks qualitatively as an intermediate case between the maps obtained from daily SAT data with $\tau = 31$ days and $\tau = 99$ days.

Chapter 6

Correlations and synchronisation in SAT time series

In this chapter we analyse raw (unfiltered) SAT time series from ERA-Interim reanalysis dataset. We study how SAT anomaly, amplitude, phase and frequency in different geographical sites are statistically correlated.

Firstly, in section 6.1 we investigate SAT dynamics from the point of view of coupled oscillators characterised only by their phases. In this framework, we use the Kuramoto parameter [79, 80] to quantify synchronisation within three different regions: northern extratropics, southern extratropics and the tropics. We calculate this quantity because we could use its temporal evolution as an indicator of large-scale climate phenomena such as El Niño. In fact, it has been shown that episodes of El Niño affect the connectivity of the climate network [19–21]. We find the extratropics to have higher synchronisation than the tropics, which is the expected results since in the extratropics the annual oscillation of SAT is stronger.

Then, in section 6.2 we calculate the Pearson correlations between pairs of sites, using different time series. Specifically, we consider the time series of SAT anomaly and three series obtained by HT: phase, amplitude and frequency. The analysis of correlation values between the cosine of the phase confirms the results obtained with Kuramoto parameter. We see that sites in the extratropics are strongly correlated, while sites in the tropics have weaker correlations. As a next step, comparing the correlation values obtained from SAT anomaly, amplitude and frequency, we can appreciate different correlation patterns. We interpret these findings as due to different time scales of the main climatic

phenomena: while extratropical SAT dynamics is dominated by the annual cycle, tropical SAT dynamics is dominated by variability modes with much shorter time scales. In addition, in the analysis of the extratropical sites with time lag, we find a direction of flow of information, which is explained in terms of Rossby waves.

Finally, in section 6.3 we compare the maps given by the Pearson (linear) correlation with the maps given by the Spearman (nonlinear) correlation and see that the results are almost the same. This suggests that the correlation patterns that we have found have mainly a linear origin.

The results that we present in this chapter will be summarised in a manuscript that will be submitted for publication.

6.1 Synchronisation

As a first approach to search for similarities in SAT dynamics between different sites, we quantify their degree of synchronisation. We consider the SAT dynamics in the sites as representing a system of coupled oscillators, each one characterised by its own phase $\varphi_j(t)$.

SAT oscillations give different seasons in the two extratropics and in the tropics, thus we divide the world into three wide geographical areas:

- *northern extratropics*: sites to the north of 30°;
- *southern extratropics*: sites to the south of −30°;
- *tropics*: sites between −30° and 30°.

Our aim is to quantify the synchronisation in these three areas. To do that, in each area S we calculate the Kuramoto parameter as a function of time. We take into account the weight w_j of each site, proportional to its area, so the Kuramoto parameter is given by

$$r(t) = \left| r(t) e^{i\psi(t)} \right| = \left| \frac{\sum\limits_{j \in S} w_j e^{i\varphi_j(t)}}{\sum\limits_{j \in S} w_j} \right| . \tag{6.1}$$

Here $r(t)$ represents synchronisation as the phase coherence of the set of oscillators, while $\psi(t)$ is the average phase. The parameter $r(t)$ takes values in the interval $[0, 1]$: from total desynchronisation (phases uniformly distributed in the interval $[0, 2\pi]$) to total synchronisation (all equal phases).

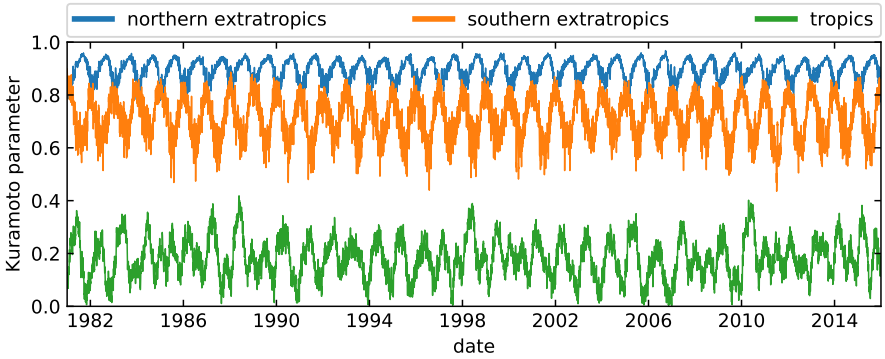

Figure 6.1: Evolution of the Kuramoto parameter for the three geographical areas: northen extratropics, southern extratropics and tropics.

The results are shown in figure 6.1. We find a high synchronisation in the northern extratropics, a slightly lower synchronisation in the southern extratropics, and almost no synchronisation in the tropics. We also note a seasonal variation in synchronisation, with an oscillation that is wider in the southern extratropics than in the northern extratropics. Also, the extratropics have a higher synchronisation in their summer than in their winter.

A relevant question is whether the synchronisation parameter can be an indicator of climate phenomena such as El Niño. To investigate this possibility, for each of the three regions we compare its Kuramoto series with the Niño 3.4 index ([104]), for time lags between -12 months and 12 months. The results (not reported here) do not reveal any significative correlation.

6.2 Linear correlation

The next step is to calculate the statistical similarity between time series of different sites. We consider time series of four different variables: SAT anomaly, amplitude, frequency and cosine of the phase. For each pair of sites, i and j, we calculate the Pearson correlation coefficient between the time series of the same variable. If we use, for example, frequency time series, the correlation is

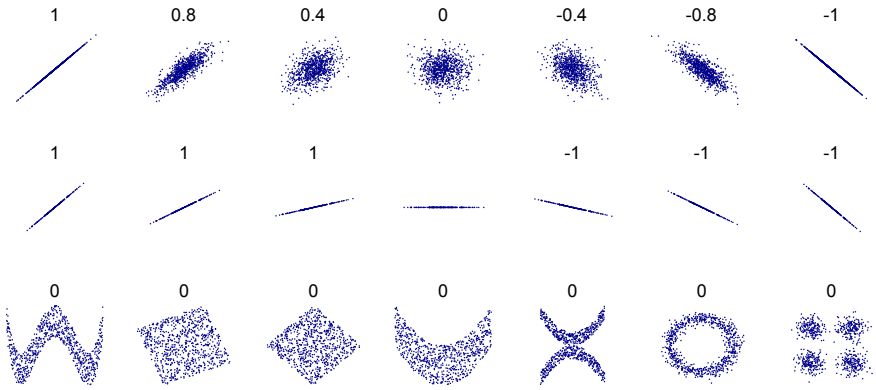

Figure 6.2: Examples of Pearson correlation coefficients between x and y for several sets of points. The top row illustrates how the coefficient value reflects the presence of linear correlation. The second row illustrates how the slope only influences the sign of the coefficient, but not the value. The third row illustrates that the Pearson coefficient cannot detect many types of nonlinear correlations. Taken from [105].

given by the expression

$$r_{ij} = \frac{\sum_t \left[\omega_i(t) - \overline{\omega}_i\right]\left[\omega_j(t-l) - \overline{\omega}_j\right]}{\sqrt{\sum_t \left[\omega_i(t) - \overline{\omega}_i\right]^2}\sqrt{\sum_t \left[\omega_j(t) - \overline{\omega}_j\right]^2}}. \tag{6.2}$$

This formula searches for linear correlation between the two time series, with time lag l. In fact, the sum in the numerator compares ω_i at time t with ω_j at time $t-l$. Figure 6.2 shows the properties of the Pearson correlation coefficient. It takes values in the interval $[-1, 1]$ and quantifies the linear correlation between the two time series ω_i and ω_j. The value $r_{ij} = 1$ indicates perfect positive correlation: if we draw a scatter plot of the two series, the points lie exactly on a straight ascending line. More in general, $0 < r_{ij} < 1$ means that the points approximately lie on a straight ascending line. Analogously, negative values of r_{ij} indicate negative correlation: points lying on a straight descending line. The case $r_{ij} = 0$ indicates that there is no linear correlation between the two time series. In principle there could be nonlinear correlation, which would not be detected by the Pearson correlation coefficient. To explore this possibility, in section 6.3 we search also for nonlinear correlation using the

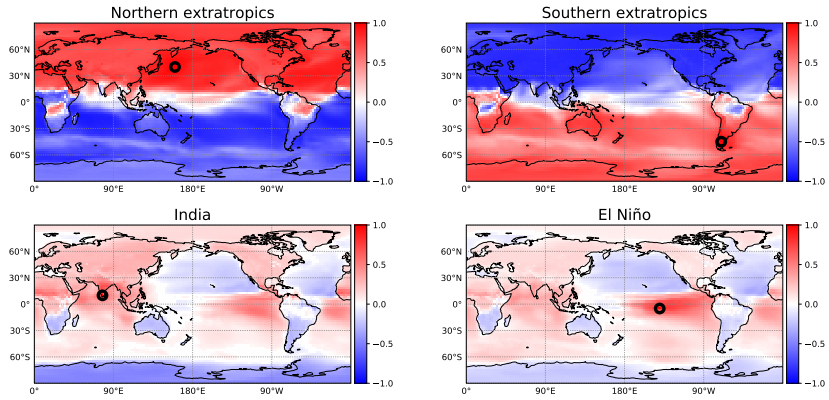

Figure 6.3: Correlation maps of the four chosen sites, calculated from the Pearson coefficient between time series of the cosine of the phase. In each map, the chosen site is marked with a circle and its correlations with the rest of the world are represented according to the indicated colour scale. The four sites are: northern extratropics (40 N, 160 E), southern extratropics (45 S, 70 W), India (10 N, 77.5 E), El Niño (5 S, 140 W).

Spearman coefficient and we obtain very similar results to the ones obtained with the Pearson coefficient.

We apply the formula 6.2 and calculate the correlation values between each pair of sites. We point out that it is also important to evaluate the statistical significance of the obtained correlation value. A possible way to do this (left for future work) is to generate subrogate time series (uncorrelated between them, but keeping the autocorrelation properties of each individual time series [38, 106, 107]), then calculate correlations on them, and finally compute statistics over the set of subrogated correlation values.

To view the patterns of correlation, we select four specific geographical sites and see how they are correlated with the rest of the world. The four sites, as indicated in figure 6.3, are: one in the northern extratropics, in north Pacific Ocean; one in the southern extratropics, in southern South America; and two in the tropics, one in India and the other one in central Pacific Ocean.

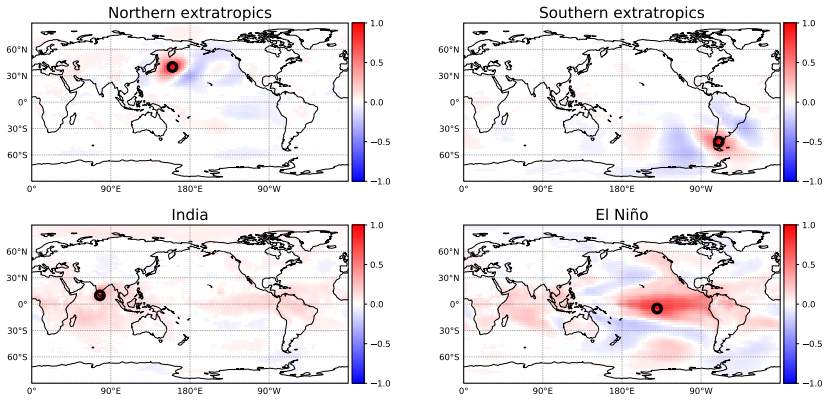

Figure 6.4: Correlation maps of the four chosen sites, analogous to those in fig. 6.3, calculated from anomaly series.

6.2.1 Linear correlation without time lag

First of all, to confirm the results found with the Kuramoto parameter, we explore the correlations of the four sites, without time lag, calculated from the time series of cosine of the phase. This time series expresses the evolution of seasonal oscillation, so we expect a strong correlation between sites whose SAT oscillations are in phase. For each of the four sites we show its correlation map, where colours indicate the strength of the correlation (Pearson coefficient) between the given site and the rest of the world. The results, presented in figure 6.3, confirm what we found with the Kuramoto parameter: strong correlations in the extratropics and weaker correlations in the tropics.

Then, we explore the correlations of the same four sites, without time lag, using the other time series: SAT anomaly, amplitude and frequency. Anomaly (figure 6.4) gives strong correlation patterns in the extratropical sites, with bands of opposite signs, and in the El Niño site; it gives weaker correlations in the Indian site. Amplitude (figure 6.5) gives strong correlation patterns in all four sites. Also, in the extratropical sites there are qualitative similarities between the maps given by anomaly and amplitude. Frequency (figure 6.6) gives, in the extratropical sites, patterns of correlation that are qualitatively similar to the ones given by anomaly, albeit weaker. On the other hand, in the two tropical sites, frequency gives much lower values of correlation, without any clear pattern.

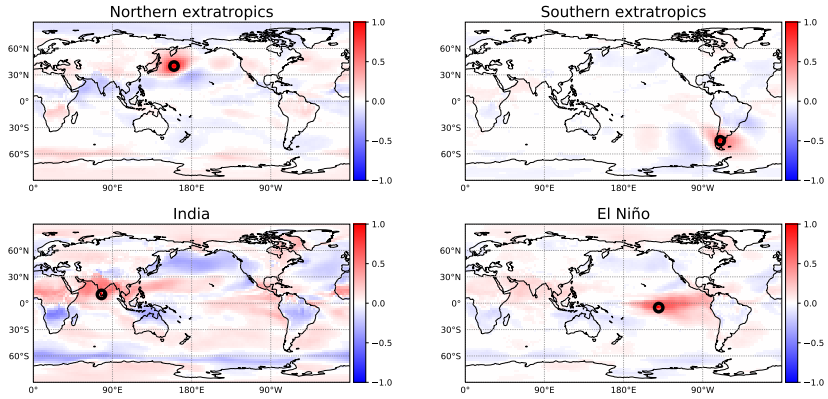

Figure 6.5: Correlation maps of the four chosen sites, analogous to those in fig. 6.3, calculated from amplitude series.

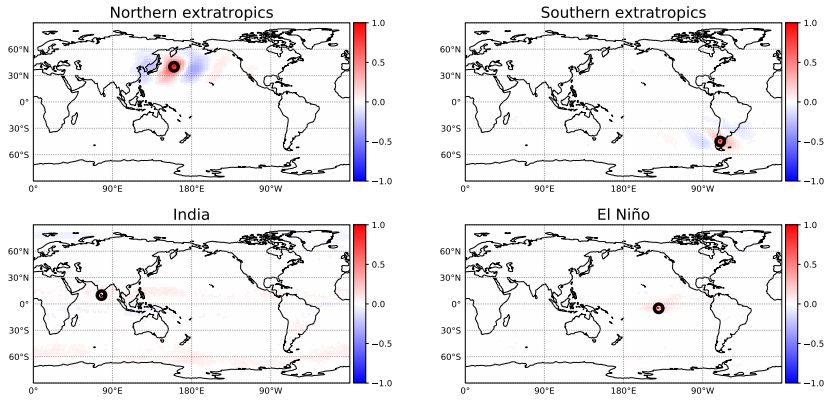

Figure 6.6: Correlation maps of the four chosen sites, analogous to those in fig. 6.3, calculated from frequency series.

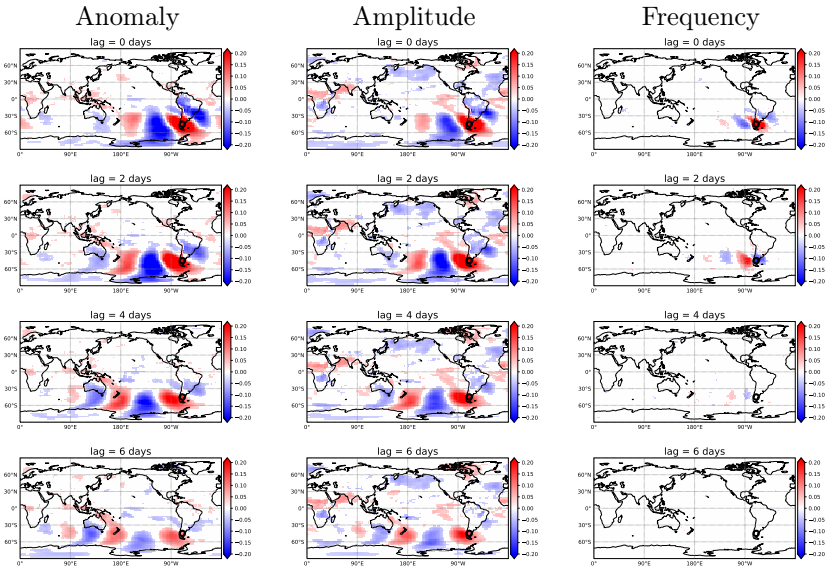

Figure 6.7: Correlation maps of the site in southern extratropics, given by the Pearson coefficient applied to 3 different time series (indicated at the top of each column), with different time lags l. We compare the given site at time t with the rest of the world at time $t - l$.

6.2.2 Linear correlation with time lag

Here we consider a time lag in the calculation of the Pearson correlation. In particular, when we calculate the correlation map of a site, we compare the given site at time t with the rest of the world at time $t - l$. In other words, we find how climate in the given site is correlated with past climate of other regions.

The results are reported in figure 6.7 for the time series of anomaly, amplitude and frequency. We can see that in the three cases the pattern of correlation shifts toward the west with increasing lag.

6.3 Nonlinear correlation

As explained in section 6.2, the Pearson correlation coefficient only detects linear correlations. To search for the presence of nonlinear correlations, we need to

use other indicators, such as the Spearman correlation coefficient or the mutual information. In this section, we use the Spearman coefficient, that measures the monotonic correlation between the two series, be it linear or nonlinear. Its calculation is analogous to the calculation of the Pearson correlation (eq. 6.2), but the actual values of the series are substituted by their ranks. That is, if we consider for example the time series ω_j and sort all its values, at each instant t we take the ranking $k_j(t)$ of the value $\omega_j(t)$. So, the Spearman correlation coefficient ρ is given by

$$\rho_{ij} = \frac{\sum_t \left[k_i(t) - \overline{k}_i\right]\left[k_j(t-l) - \overline{k}_j\right]}{\sqrt{\sum_t \left[k_i(t) - \overline{k}_i\right]^2}\sqrt{\sum_t \left[k_j(t) - \overline{k}_j\right]^2}}. \tag{6.3}$$

It measures how well the relationship between the two series can be described by a monotonic function. It takes values in the interval $[-1, 1]$. The two extreme values indicate that the relationship can be described by a perfectly monotonic function. The null value indicates that there is no monotonic relationship between the two time series.

In figure 6.8 we show the comparison between the correlation maps given by the Pearson correlation and those given by the Spearman correlation, calculated for the four sites with no time lag. In particular, we present correlations between amplitude series. We can see that we obtain almost exactly the same correlation maps with the two correlation measures. If we repeat the same comparison using the other time series, we also find that the two correlations give nearly identical maps. This indicates us that the correlations between the time series in different sites are essentially linear. Similar results have been found for anomaly time series by other researches [108].

6.4 Discussion

In this chapter, we have used Hilbert analysis to study the similarities between SAT dynamics in different regions. We have characterised these similarities by synchronisation and statistical correlation.

First, we calculated the Kuramoto parameter using the time series of the Hilbert phase, to measure synchronisation in three regions of the world. We found that both extratropics have a high degree of synchronisation, with northern extratropics being slightly more synchronous than southern extratropics. In contrast, the tropical region has a low degree of synchronisation. The aim of this analysis was to relate a global synchronisation measure with a climate

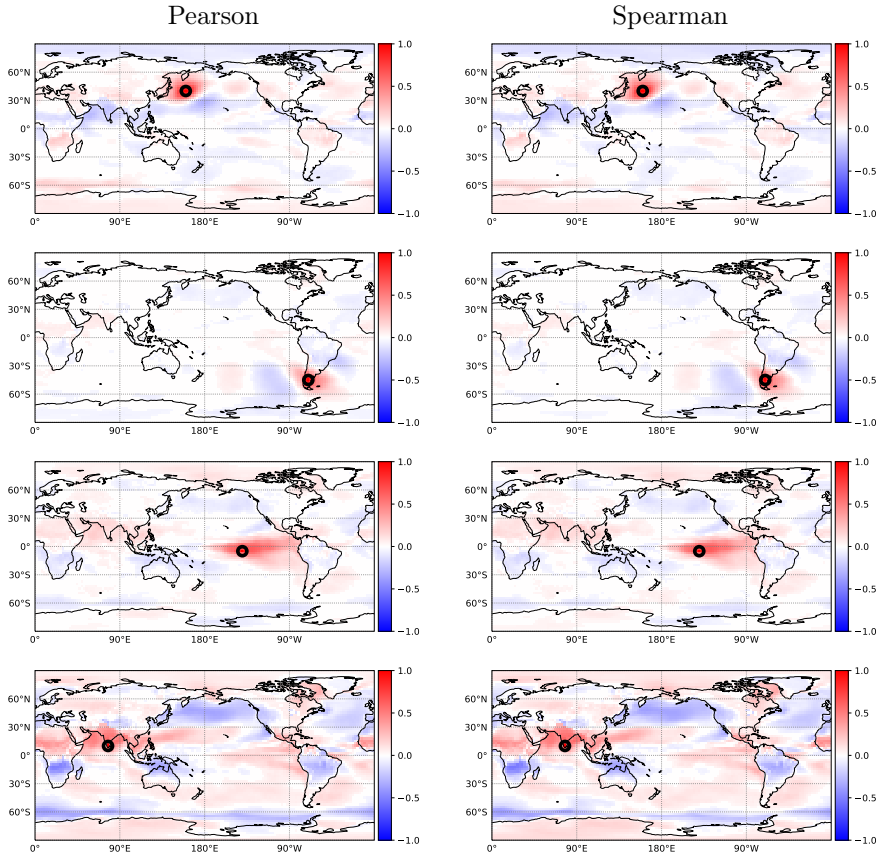

Figure 6.8: Comparison between the correlation maps given by Pearson and Spearman correlations. For each of the four chosen sites (as in fig. 6.3), we calculate the two correlation maps using the amplitude series. Left column reports the Pearson correlations, while right column reports the Spearman correlations.

phenomenon such as El Niño. We searched for linear correlations between the Kuramoto series and the Niño 3.4 index, but only weak and non-significative correlations were found. Further studies are needed to understand the origin of the fluctuations seen in the Kuramoto parameter and to select different geographical regions where the parameter is calculated.

Then, we analysed Pearson correlations between the time series of the cosine of the phase. In this way, a strong correlation between two sites indicates that their SAT oscillations are in phase. We found that both extratropics have high values of correlation: the sites of the same extratropics are strongly in phase, while they are in phase opposition with the sites of the other extratropics. In contrast, the region of the tropics has lower values of correlation.

These are expected results that can be easily interpreted: in the extratropics, SAT dynamics are similar since they are dominated by the common annual cycle; on the other hand, in the tropics the annual cycle is weak and SAT is also determined by local faster variability modes, so distant sites are not necessarily in phase. The stronger synchronisation of the northern extratropics compared to the southern extratropics can be explained by the presence in the northern extratropics of larger landmasses, that give an annual cycle of SAT with a wider amplitude. Another factor that can account for the higher synchronisation of the northern extratropics is the presence in the atmosphere of standing waves with higher amplitude. These waves are generated by the interaction between atmospheric circulation and topography, so they are influenced by the presence of larger landmasses.

Then, we explored the correlation obtained from the other time series: SAT anomaly, amplitude and frequency. We found that anomaly gives strong correlation patterns in both extratropics and in the El Niño site, and weaker correlations in the Indian site. In the extratropical sites, we can see correlation patterns formed by bands of alternating signs. These patterns are produced by Rossby waves, as we will discuss more in depth. The tropics have a different dynamics, since local processes of deep convection dominate SAT anomaly, thus giving low synchronisation between distant sites. As for the correlation pattern of the El Niño site, its long range correlations can be explained by the ENSO oscillation, which has been proved to have strong influence over different regions in the world [12, 19–21, 64, 109].

It is well known that patterns of correlation in the extratropics are produced mainly by Rossby waves [12, 45, 110]. That happens because Rossby waves produce meanders in the jet streams, which cause anomalies in SAT with coherent spatial structures. An evidence for this comes if we analyse the maps of correlation with time lag in the southern extratropical site. We find that

the patterns of correlation move eastward as we reduce the time lag, which is compatible with the direction of the jet streams. In fact, as a Rossby wave propagates eastward, the pattern of SAT anomaly that it generates travels together with the wave.

Amplitude gives strong correlation patterns in the four sites. There are similarities with the correlation given by anomaly, especially in the extratropical sites, but there are also substantial differences, especially in the Indian site. We know that, by construction, if the SAT seasonal cycle is not a perfect sinusoid (and actually it is not), the amplitude is not constant and contains an oscillating mode that comes from the deviation of SAT from the sinusoidal oscillation. So, we speculate that this oscillating mode can explain the differences between the correlation patterns given by anomaly and by amplitude, since anomaly does not contain that mode.

Frequency gives in the extratropics a similar correlation pattern to the one given by anomaly, even if weaker; but it gives almost no significative correlations in the tropical sites. This difference is explained by the fact that, in the tropics, the seasonal SAT oscillation is small and frequency is mainly determined by fast fluctuations (faster than seasonal oscillations). Thus, frequency does not take into account annual oscillations and slower oscillations, such as ENSO, that can produce long range correlations in SAT anomaly.

To summarise, in this chapter we have seen that the time series that we obtain from the Hilbert transform have correlations that capture actual climate phenomena, such as SAT seasonal oscillation patterns, ENSO oscillation and Rossby waves. A possible future development of this study is using these correlations to build climate networks and trying to extract from these networks indicators of climate phenomena.

Chapter 7

Conclusions

7.1 Summary

In this thesis we have demonstrated that the Hilbert transform can be used in several ways as a tool to analyse climate time series. When applied to an oscillating signal, the HT allows us to calculate the instantaneous amplitude, phase and frequency of the signal. These series are the starting point of our analysis techniques. We have also pointed out that the HT has some limitations, mainly the fact that the amplitude and phase time series have the physical meaning of rotation only when the initial signal has a narrow band of frequency. However, we have showed that it is possible to find meaningful results even from raw SAT series with a wide band of frequencies. In particular, we were able to uncover spatial patterns of average frequency, to quantify interdecadal changes in SAT dynamics and to find correlation and synchronisation between different geographical sites. On the other hand, by applying a smoothing filter and varying the length of the averaging window, we were able to characterise different SAT dynamics and to identify different climatic regions.

In chapter 3 we started by analysing the instantaneous frequency calculated from SAT time series and found well-defined spatial patterns. In the extratropics, the average frequency in general has the expected value of one oscillation per year, produced by the annual cycle of solar forcing. On the other hand, the tropics in general have higher frequencies, since in this region the seasonal oscillation of temperature is small in comparison to more rapid fluctuations caused by other climatic phenomena. We also found well-defined patterns of standard deviation of frequency, that largely coincide with regions of high

precipitation. In addition, in the extratropics, the average value of frequency and its standard deviation tend to be higher in winter than in summer. This happens because, in the midlatitude oceans, the air-sea contrast is larger in winter than in summer, and SST gradients are larger. So, the atmosphere allows faster changes in SAT fluctuations and higher day-to-day variability.

We also analysed the evolution of frequency in specific geographical sites and saw that frequency has an irregular behaviour with large fluctuations. Instead of applying a filter on SAT to obtain a narrow band of frequency, we showed that frequency fluctuations contain meaningful information about large-scale climate phenomena. Our results indicate that Hilbert analysis can be a valuable tool to gain information about the dynamics of climatic variables.

In chapter 4 we used the time series of amplitude and frequency to study changes in SAT dynamics over the last 35 years. We calculated the relative change, between the first and the last decade, of the average and standard deviation of amplitude and frequency. Using the series of amplitude, we found the highest values of change (more than 50%) in Amazonia and in the Arctic. They can be interpreted, respectively, as due to precipitation decrease and to ice melting. Analysing the series of frequency, we found high values of change (more than 100%) in the Pacific Ocean: two areas of opposite sign in the eastern part and two areas of increase in the western part. These findings were interpreted as due to a shift towards north and a widening of the ITCZ. Confirming the shift of the ITCZ is an important result because its migration can have far-reaching consequences on the Earth's climate.

We also performed different analyses to test the robustness of our findings. We saw that, changing the threshold of the significance test, the main areas of change remain unaffected. Secondly, changing the length of the interval over which we calculate the relative change, the patterns of change conserve the same shape. Lastly, we compared the results obtained from the two datasets and found very similar structures. The few discrepancies were interpreted as due to differences in the datasets, likely the consequences of the two different reanalysis models.

In chapter 5 we used Hilbert analysis to unveil hidden regularities in SAT dynamics and to characterise different types of dynamics. We smoothed the SAT series, then calculated its instantaneous phase and from the phase we calculated the mean period of rotation. We analysed plots of the mean period as a function of the smoothing length and found well-defined plateaus, which reveal hidden regularities of SAT dynamics. We also showed that these results cannot be obtained by Fourier analysis, because the dominant peak of the spectrum has a frequency that is either constant or changes abruptly. We

used a well-known machine learning algorithm, k-means, to classify the sites in four clusters according to their values of mean period as a function of the smoothing length. The classification that we found actually reflects different climatic regions. Our results demonstrate that Hilbert analysis, combined with temporal averaging, can be used to uncover hidden temporal regularities and for the classification of different oscillatory behaviours.

To corroborate our results, we performed the same analysis on data generated by a synthetic model. We found that the mean period depends on the smoothing length in a way that is fully consistent with the model and the parameters used to generate the synthetic data. In addition, with the simple model it was possible to reproduce the dependence of the mean period found in four sites. We also compared the results given by two datasets and found in many cases the same dependence of the mean period. The discrepancies were interpreted as due to different grid resolutions of the two datasets, that become evident in regions with a high gradient of climatic behaviour. Finally, to analyse the influence of the sampling time, we calculated the map of mean period from SAT data with monthly resolution and found results that are consistent with the smoothed daily data.

In chapter 6 we investigated the similarities between SAT dynamics in different regions. Firstly we measured the synchronisation of the phase in three geographical areas: we found that both extratropics are highly synchronised, while the tropics are poorly synchronised. We also confirmed these results by analysing the statistical correlations between the time series of the cosine of the phase. We found that both extratropics have high values of correlation: the sites of the same extratropics are strongly in phase, while they are in phase opposition with the sites in the other extratropics. On the other hand, the tropics have low values of phase correlation. It is easy to interpret these results: as we expected, in the extratropics SAT dynamics is dominated by the annual cycle, hence the strong synchronisation. In contrast, in the tropics the annual cycle is weak and SAT dynamics is dominated by local faster variability modes, hence the weak synchronisation.

Then, we analysed the connectivities of several sites using the time series of SAT anomaly, amplitude and frequency. We found similarities and differences that could be explained by the characteristics of the climate in the different regions. Anomaly gives in the extratropics peculiar patterns of connectivity that are mainly due to Rossby waves. Studying the connectivity with time lag, we found an eastward shift of the pattern that confirms our interpretation. In the tropics, anomaly gives a connectivity pattern that is influenced by ENSO. Amplitude gives a strong connectivity in all the analysed sites. We

speculated that this is due to the fact that amplitude contains an annual oscillation, while SAT anomaly does not. Frequency gives in the extratropics a connectivity similar to the one given by anomaly, but in the tropics it gives almost no significant correlations. This was interpreted as due to the fact that in the tropics frequency is mainly determined by fast (faster than the annual oscillation) and local fluctuations, instead of the annual or slower oscillations (such as ENSO) that can produce long range correlations.

7.2 Future perspectives

The work presented in this thesis leaves several open questions, which can be explored in future research. First of all, we applied the Hilbert transform to time series of surface air temperature. There are many other climatic time series that can exhibit interesting oscillating dynamics, such as surface sea temperature, pressure and precipitation. In particular, using other time series, it could be possible to better characterise the interdecadal changes in climate dynamics and to identify and quantify their impacts.

We used the dependence of the mean period on the smoothing length to characterise SAT dynamics in different sites. An interesting possibility would be to use other time series calculated from Hilbert transform to characterise the dynamics of climate. Also, when searching for a classification of the sites based on their features, we could use other classification algorithms. In general, choosing different features and changing the classification algorithms, it could be possible to find classifications that reflect differences and analogies between various climatic aspects.

Regarding our work on correlations between time series, its natural continuation would be to use these correlations to build a climate network. There are many possible approaches to calculate the correlations and then there are different ways to select only significant correlation values as links in the network. Once the network is built, it is possible to perform some global and local measures on it. Our idea would be to use these measures as indicators of some climate phenomena, such as El Niño or monsoons. Another possibility with climate networks is to calculate directionality measures, to study how the effects of climate phenomena propagate on the globe. Also, it could be interesting to separate data according to seasons or some climatic indicator and calculate separate climate networks. In this case, analysing the differences between the networks, it could be possible to gain new insights for better understanding our climate. Another line of research could be to apply a smoothing filter to the

initial SAT series and study how this influences the structure of the network. Also, we could explore the possibility of searching for correlations between different variables calculated by HT.

Finally, an interesting application would be to use Hilbert time series to progress in the predictability of the original time series and their extreme fluctuations. In the same way, Hilbert time series could contribute to the predictability of climate indices (such as El Niño 3.4), by searching for correlations between a given index and quantities calculated from Hilbert analysis.

Bibliography

[1] M. Ghil, P. Yiou, S. Hallegatte *et al.*, "Extreme events: dynamics, statistics and prediction", *Nonlinear Processes in Geophysics*, vol. 18, pp. 295–350, 2011. DOI: 10.5194/npg-18-295-2011.

[2] O. Lejeune, M. Tlidi and P. Couteron, "Localized vegetation patches: a self-organized response to resource scarcity", *Physical Review E*, vol. 66, no. 1, p. 010 901, 2002. DOI: 10.1103/PhysRevE.66.010901.

[3] L. J. Beaumont, A. Pitman, S. Perkins *et al.*, "Impacts of climate change on the world's most exceptional ecoregions", *Proceedings of the National Academy of Sciences*, vol. 108, no. 6, pp. 2306–2311, 2011. DOI: 10.1073/pnas.1007217108.

[4] M. Gottfried, H. Pauli, A. Futschik *et al.*, "Continent-wide response of mountain vegetation to climate change", *Nature Climate Change*, vol. 2, no. 2, pages 111–115, 2012. DOI: 10.1038/nclimate1329.

[5] I. Bordeu, M. G. Clerc, P. Couteron *et al.*, "Self-replication of localized vegetation patches in scarce environments", *Scientific Reports*, vol. 6, p. 33 703, 2016. DOI: 10.1038/srep33703.

[6] S. Albeverio, V. Jentsch and H. Kantz, *Extreme events in nature and society*. Springer, 2006, ISBN: 978-3-540-28610-3.

[7] M. Barreiro, A. Fedorov, R. Pacanowski and S. G. Philander, "Abrupt Climate Changes: How Freshening of the Northern Atlantic Affects the Thermohaline and Wind-Driven Oceanic Circulations", *Annual Review of Earth and Planetary Sciences*, vol. 36, pp. 33–58, 2008. DOI: 10.1146/annurev.earth.36.090507.143219.

[8] D. Coumou and S. Rahmstorf, "A decade of weather extremes", *Nature Climate Change*, vol. 2, no. 7, pp. 491–496, 2012. DOI: 10.1038/NCLIMATE1452.

[9] M. H. England, S. McGregor, P. Spence *et al.*, "Recent intensification of wind-driven circulation in the Pacific and the ongoing warming hiatus", *Nature Climate Change*, vol. 4, no. 3, pp. 222–227, 2014. DOI: 10.1038/nclimate2106.

[10] W. Cai, S. Borlace, M. Lengaigne *et al.*, "Increasing frequency of extreme El Niño events due to greenhouse warming", *Nature Climate Change*, vol. 4, no. 2, pp. 111–116, 2014. DOI: 10.1038/NCLIMATE2100.

[11] M. Turco, E. Palazzi, J. von Hardenberg and A. Provenzale, "Observed climate change hot-spots", *Geophysical Research Letters*, vol. 42, no. 9, pp. 3521–3528, 2015. DOI: 10.1002/2015GL063891.

[12] H. A. Dijkstra, *Nonlinear Climate Dynamics*. Cambridge University Press, 2013, ISBN: 9781139034135.

[13] M. Ghil, "Natural Climate Variability", in *Encyclopedia of Global Environmental Change*, T. Munn, Ed. John Wiley & Sons, 2002, vol. 1, pp. 544–549, ISBN: 0-471-97796-9.

[14] W. F. Ruddiman, "Orbital changes and climate", *Quaternary Science Reviews*, vol. 25, no. 23–24, pp. 3092–3112, 2006. DOI: 10.1016/j.quascirev.2006.09.001.

[15] P. D. Ditlevsen and P. Ashwin, "Complex climate response to astronomical forcing: The middle-Pleistocene transition in glacial cycles and changes in frequency locking", *Frontiers in Physics*, vol. 6, p. 62, 2018. DOI: 10.3389/fphy.2018.00062.

[16] J. Bjerknes, "A possible response of the atmospheric Hadley circulation to equatorial anomalies of ocean temperature", *Tellus*, vol. 18, no. 4, pp. 820–829, 1966.

[17] ——, "Atmospheric Teleconnections from the Equatorial Pacific", *Monthly Weather Review*, vol. 97, no. 3, pp. 163–172, 1969.

[18] R. Brakenridge *et al.* (2008). Dartmouth Flood Observatory, [Online]. Available: http://www.dartmouth.edu/~floods/ONI.png (visited on 22/01/2019).

[19] A. Gozolchiani, K. Yamasaki, O. Gazit and S. Havlin, "Pattern of climate network blinking links follows El Niño events", *Europhysics Letters*, vol. 83, no. 2, p. 28 005, 2008. DOI: 10.1209/0295-5075/83/28005.

[20] K. Yamasaki, A. Gozolchiani and S. Havlin, "Climate Networks around the Globe are Significantly Affected by El Niño", *Physical Review Letters*, vol. 100, no. 22, p. 228 501, 2008. DOI: 10.1103/PhysRevLett.100.228501.

[21] A. A. Tsonis and K. L. Swanson, "Topology and Predictability of El Niño and La Niña Networks", *Physical Review Letters*, vol. 100, no. 22, p. 228 502, 2008. DOI: 10.1103/PhysRevLett.100.228502.

[22] P. Graystone, "Meteorological office discussion on tropical meteorology", *Meteorological Magazine*, vol. 88, pp. 113–119, 1959.

[23] R. A. Ebdon, "Notes on the wind flow at 50 mb in tropical and subtropical regions in January 1957 and January 1958", *Quarterly Journal of the Royal Meteorological Society*, vol. 86, no. 370, pp. 540–542, 1960. DOI: 10.1002/qj.49708637011.

[24] M. Paluš and D. Novotná, "Quasi-biennial oscillations extracted from the monthly NAO index and temperature records are phase-synchronized", *Nonlinear Processes in Geophysics*, vol. 13, no. 3, pp. 287–296, 2006. DOI: 10.5194/npg-13-287-2006.

[25] A. G. Marshall and A. A. Scaife, "Impact of the QBO on surface winter climate", *Journal of Geophysical Research*, vol. 114, no. D18110, 2009. DOI: 10.1029/2009JD011737.

[26] M. Takahashi, "Simulation of the stratospheric Quasi-Biennial Oscillation using a general circulation model", *Geophysical Research Letters*, vol. 23, no. 6, pp. 661–664, 1996. DOI: 10.1029/95GL03413.

[27] A. A. Scaife, N. Butchart, C. D. Warner *et al.*, "Realistic quasi-biennial oscillations in a simulation of the global climate", *Geophysical Research Letters*, vol. 27, no. 1, pp. 3481–3484, 2000. DOI: 10.1029/2000GL011625.

[28] M. A. Giorgetta, E. Manzini and E. Roeckner, "Forcing of the quasi-biennial oscillation from a broad spectrum of atmospheric waves", *Geophysical Research Letters*, vol. 29, no. 8, pp. 86-1–86-4, 2002. DOI: 10.1029/2002GL014756.

[29] R. G. Barry and R. J. Chorley, *Atmosphere, Weather, and Climate*. Routledge, 2009, ISBN: 978-0415465700.

[30] R. A. Madden and P. R. Julian, "Detection of a 40–50 day oscillation in the zonal wind in the tropical Pacific", *Journal of Atmospheric Sciences*, vol. 28, no. 5, pp. 702–708, 1971.

[31] ——, "Description of global-scale circulation cells in the tropics with a 40–50 day period", *Journal of Atmospheric Sciences*, vol. 29, no. 6, pp. 1109–1123, 1972.

[32] C.-G. Rossby and collaborators, "Relation between variations in the intensity of the zonal circulation of the atmosphere and the displacements of the semi-permanent centers of action", *Journal of Marine Research*, vol. 2, no. 1, pp. 38–55, 1939.

[33] G. W. Platzman, "The Rossby wave", *Quarterly Journal of the Royal Meteorological Society*, vol. 94, no. 401, p. 225, 1968. DOI: 10.1002/qj.49709440102.

[34] K. E. Trenberth, *Climate System Modeling*. Cambridge University Press, 1993, ISBN: 9780521432313.

[35] M. Claussen, L. A. Mysak, A. J. Weaver *et al.*, "Earth system models of intermediate complexity: closing the gap in the spectrum of climate system models", *Climate Dynamics*, vol. 18, no. 7, pp. 579–586, 2002. DOI: 10.1007/s00382-001-0200-1.

[36] P. Bauer, A. Thorpe and G. Brunet, "The quiet revolution of numerical weather prediction", *Nature*, vol. 525, pp. 47–55, 2015. DOI: 10.1038/nature14956.

[37] A. J. Simmons, P. Poli, D. P. Dee *et al.*, "Estimating low-frequency variability and trends in atmospheric temperature using ERA-Interim", *Quarterly Journal of the Royal Meteorological Society*, vol. 140, no. 679, pp. 329–353, 2014. DOI: 10.1002/qj.2317.

[38] M. Mudelsee, *Climate Time Series Analysis*. Springer, 2014, ISBN: 978-3-319-04450-7.

[39] N. Boers, B. Goswami, A. Rheinwalt *et al.*, "Complex networks reveal global pattern of extreme-rainfall teleconnections", *Nature*, 2019. DOI: 10.1038/s41586-018-0872-x.

[40] J. Ludescher, A. Gozolchiani, M. I. Bogachev *et al.*, "Very early warning of next El Niño", *Proceedings of the National Academy of Sciences*, vol. 111, no. 6, pp. 2064–2066, 2014. DOI: 10.1073/pnas.1323058111.

[41] N. Boers, B. Bookhagen, H. M. J. Barbosa *et al.*, "Prediction of extreme floods in the eastern Central Andes based on a complex networks approach", *Nature Communications*, vol. 5, p. 5199, 2014. DOI: 10.1038/ncomms6199.

[42] V. Stolbova, E. Surovyatkina, B. Bookhagen and J. Kurths, "Tipping elements of the Indian monsoon: Prediction of onset and withdrawal", *Geophysical Research Letters*, vol. 43, no. 8, pp. 3982–3990, 2016. DOI: 10.1002/2016GL068392.

[43] V. Rodríguez-Méndez, V. M. Eguíluz, E. Hernández-García and J. J. Ramasco, "Percolation-based precursors of transitions in extended systems", *Scientific Reports*, vol. 6, p. 29 552, 2016. DOI: 10.1038/srep29552.

[44] J. Pathak, B. Hunt, M. Girvan *et al.*, "Model-free prediction of large spatiotemporally chaotic systems from data: A reservoir computing approach", *Physical Review Letters*, vol. 120, no. 2, p. 024 102, 2018. DOI: 10.1103/PhysRevLett.120.024102.

[45] M. Gelbrecht, N. Boers and J. Kurths, "Phase coherence between precipitation in South America and Rossby waves", *Science Advances*, vol. 4, no. 12, eaau3191, 2018. DOI: 10.1126/sciadv.aau3191.

[46] P. D. Nooteboom, Q. Y. Feng, C. López *et al.*, "Using network theory and machine learning to predict El Niño", *Earth System Dynamics*, vol. 9, no. 3, pp. 969–983, 2018. DOI: 10.5194/esd-9-969-2018.

[47] E. Koscielny-Bunde, A. Bunde, S. Havlin *et al.*, "Indication of a Universal Persistence Law Governing Atmospheric Variability", *Physical Review Letters*, vol. 81, no. 3, pp. 729–732, 1998. DOI: 10.1103/PhysRevLett.81.729.

[48] N. Kalamaras, K. Philippopoulos, D. Deligiorgi *et al.*, "Multifractal scaling properties of daily air temperature time series", *Chaos, Solitons & Fractals*, vol. 98, pp. 38–43, 2017. DOI: 10.1016/j.chaos.2017.03.003.

[49] J. A. Tenreiro Machado and A. M. Lopes, "Fractional State Space Analysis of Temperature Time Series", *Fractional Calculus and Applied Analysis*, vol. 18, no. 6, 2015. DOI: 10.1515/fca-2015-0088.

[50] S. Baliunas, P. Frick, D. Sokoloff and W. Soon, "Time scales and trends in the Central England Temperature data (1659–1990): A wavelet analysis", *Geophysical Research Letters*, vol. 24, no. 11, pp. 1351–1354, 1997. DOI: 10.1029/97GL01184.

[51] D. B. Percival and A. T. Walden, *Wavelet Methods for Time Series Analysis*. Cambridge University Press, 2000, ISBN: 978-0521685085.

[52] A. R. Stine, P. J. Huybers and I. Y. Fung, "Changes in the phase of the annual cycle of surface temperature", *Nature*, vol. 457, pp. 435–440, 2009. DOI: 10.1038/nature07675.

[53] C. Qian, C. Fu and Z. Wu, "Changes in the amplitude of the temperature annual cycle in china and their implication for climate change research", *Journal of Climate*, vol. 24, no. 20, pp. 5292–5302, 2011. DOI: 10.1175/JCLI-D-11-00006.1.

[54] J. G. Dwyer, M. Biasutti and A. H. Sobel, "Projected changes in the seasonal cycle of surface temperature", *Journal of Climate*, vol. 25, pp. 6359–6374, 2012. DOI: 10.1175/JCLI-D-11-00741.1.

[55] A. R. Stine and P. J. Huybers, "Changes in the seasonal cycle of temperature and atmospheric circulation", *Journal of Climate*, vol. 25, pp. 7362–7380, 2012. DOI: 10.1175/JCLI-D-11-00470.1.

[56] L. E. Chambers, R. Altwegg, C. Barbraud *et al.*, "Phenological changes in the southern hemisphere", *PLoS ONE*, vol. 8, no. 10, e75514, 2013. DOI: 10.1371/journal.pone.0075514.

[57] G. Wang and M. E. Dillon, "Recent geographic convergence in diurnal and annual temperature cycling flattens global thermal profiles", *Nature Climate Change*, vol. 4, no. 11, pp. 988–992, 2014. DOI: 10.1038/NCLIMATE2378.

[58] J. Duan, J. Esper, U. Büntgen *et al.*, "Weakening of annual temperature cycle over the tibetan plateau since the 1870s", *Nature Communications*, vol. 8, p. 14 008, 2017. DOI: 10.1038/ncomms14008.

[59] A. A. Tsonis, K. L. Swanson and P. J. Roebber, "What do networks have to do with climate?", *Bulletin of the American Meteorological Society*, vol. 87, no. 5, pp. 585–595, 2006. DOI: 10.1175/BAMS-87-5-585.

[60] A. A. Tsonis, K. L. Swanson and G. Wang, "On the Role of Atmospheric Teleconnections in Climate", *Journal of Climate*, vol. 21, no. 12, pp. 2990–3001, 2008. DOI: 10.1175/2007JCLI1907.1.

[61] R. V. Donner and S. M. Barbosa, *Nonlinear Time Series Analysis in the Geosciences*. Springer, 2008, ISBN: 978-3540789376.

[62] J. F. Donges, Y. Zou, N. Marwan and J. Kurths, "The backbone of the climate network", *Europhysics Letters*, vol. 87, no. 4, p. 48 007, 2009. DOI: 10.1209/0295-5075/87/48007.

[63] J. F. Donges, Y. Zou and N. Marwan, "Complex networks in climate dynamics", *European Physical Journal Special Topics*, vol. 174, no. 1, pp. 157–179, 2009. DOI: 10.1140/epjst/e2009-01098-2.

[64] M. Barreiro, A. C. Marti and C. Masoller, "Inferring long memory processes in the climate network via ordinal pattern analysis", *Chaos*, vol. 21, no. 1, p. 013 101, 2011. DOI: 10.1063/1.3545273.

[65] G. Tirabassi and C. Masoller, "Unravelling the community structure of the climate system by using lags and symbolic time-series analysis", *Scientific Reports*, vol. 6, p. 29 804, 2016. DOI: 10.1038/srep29804.

[66] N. E. Huang, Z. Shen, S. R. Long *et al.*, "The empirical mode decomposition and the Hilbert spectrum for nonlinear and non-stationary time series analysis", *Proceedings of the Royal Society A*, vol. 454, no. 1971, pp. 903–995, 1998. DOI: 10.1098/rspa.1998.0193.

[67] M. Le Van Quyen, J. Foucher, J.-P. Lachaux *et al.*, "Comparison of Hilbert transform and wavelet methods for the analysis of neuronal synchrony", *Journal of Neuroscience Methods*, vol. 111, no. 2, pp. 83–98, 2001. DOI: 10.1016/S0165-0270(01)00372-7.

[68] W. J. Freeman and L. J. Rogers, "Fine temporal resolution of analytic phase reveals episodic synchronization by state transitions in gamma EEGs", *Journal of Neurophysiology*, vol. 87, no. 2, pp. 937–945, 2002. DOI: 10.1152/jn.00254.2001.

[69] A. Pikovsky, M. Rosenblum and J. Kurths, *Synchronization: A universal concept in nonlinear sciences*. Cambridge University Press, 2003, ISBN: 978-0521533522.

[70] M. Chavez, M. Besserve, C. Adam and J. Martinerie, "Towards a proper estimation of phase synchronization from time series", *Journal of Neuroscience Methods*, vol. 154, pp. 149–160, 2006. DOI: 10.1016/j.jneumeth.2005.12.009.

[71] B. Musizza, A. Stefanovska, P. V. E. McClintock *et al.*, "Interactions between cardiac, respiratory and EEG-delta oscillations in rats during anaesthesia", *The Journal of Physiology*, vol. 580, no. 1, pp. 315–326, 2007. DOI: 10.1113/jphysiol.2006.126748.

[72] H. Luo, X. Fang and B. Ertas, "Hilbert Transform and Its Engineering Applications", *American Institute of Aeronautics and Astronautics Journal*, vol. 47, no. 4, pp. 923–932, 2009. DOI: 10.2514/1.37649.

[73] A. V. Oppenheim and R. W. Schafer, *Discrete-Time Signal Processing*. Pearson, 2010, ISBN: 978-0131988422.

[74] S. K. Mukhopadhyay, M. Mitra and S. Mitra, "ECG feature extraction using differentiation, Hilbert transform, variable threshold and slope reversal approach", *Journal of Medical Engineering & Technology*, vol. 36, no. 7, pp. 372–386, 2012. DOI: 10.3109/03091902.2012.713438.

[75] N. E. Huang and Z. Wu, "A review on Hilbert-Huang transform: Method and its applications to geophysical studies", *Reviews of Geophysics*, vol. 46, no. 2, RG2006, 2008. DOI: 10.1029/2007RG000228.

[76] N. Massei and M. Fournier, "Assessing the expression of large-scale climatic fluctuations in the hydrological variability of daily seine river flow (France) between 1950 and 2008 using Hilbert-Huang transform", *Journal of Hydrology*, vol. 448, pp. 119–128, 2012. DOI: 10.1016/j.jhydrol.2012.04.052.

[77] Y.-Y. Sun, C.-H. Chen, J.-Y. Liu *et al.*, "Instantaneous phase shift of annual subsurface temperature cycles derived by the Hilbert-Huang transform", *Journal of Geophysical Research Atmospheres*, vol. 120, pp. 1670–1677, 2015. DOI: 10.1002/2014JD022574.

[78] M. J. Reddy and S. Adarsh, "Time-frequency characterization of subdivisional scale seasonal rainfall in India using the Hilbert-Huang transform", *Stochastic Environmental Research and Risk Assessment*, vol. 30, no. 4, pp. 1063–1085, 2016. DOI: 10.1007/s00477-015-1165-7.

[79] Y. Kuramoto, "Self-entrainment of a population of coupled non-linear oscillators", in *International Symposium on Mathematical Problems in Theoretical Physics*, H. Araki, Ed. Springer, 1975, pp. 420–422, ISBN: 978-3-540-07174-7.

[80] ——, *Chemical Oscillations, Waves and Turbulence*. Springer, 1984, ISBN: 978-3-642-69691-6.

[81] J. A. Acebrón, L. L. Bonilla, C. J. Pérez Vicente *et al.*, "The Kuramoto model: A simple paradigm for synchronization phenomena", *Reviews of Modern Physics*, vol. 77, no. 1, pp. 137–185, 2005. DOI: 10.1103/RevModPhys.77.137.

[82] F. A. Rodrigues, T. K. D. Peron, P. Ji and J. Kurths, "The Kuramoto model in complex networks", *Physics Reports*, vol. 610, pp. 1–98, 2016. DOI: 10.1016/j.physrep.2015.10.008.

[83] H. Kantz and T. Schreiber, *Nonlinear time series analysis*. Cambridge University Press, 2003, ISBN: 978-0521821506.

[84] M. Paluš, "Multiscale atmospheric dynamics: Cross-frequency phase–amplitude coupling in the air temperature", *Physical Review Letters*, vol. 112, p. 078 702, 2014. DOI: 10.1103/PhysRevLett.112.078702.

[85] N. E. Huang, Z. Wu, S. R. Long *et al.*, "On instantaneous frequency", *Advances in Adaptive Data Analysis*, vol. 1, no. 2, pp. 177–229, 2009. DOI: 10.1142/S1793536909000096.

[86] E. Bradley and H. Kantz, "Nonlinear time-series analysis revisited", *Chaos*, vol. 25, no. 9, p. 097 610, 2015. DOI: 10.1063/1.4917289.

[87] D. P. Dee, S. M. Uppala, A. J. Simmons *et al.*, "The ERA-Interim reanalysis: configuration and performance of the data assimilation system", *Quarterly Journal of the Royal Meteorological Society*, vol. 137, no. 656, pp. 553–597, 2011. DOI: 10.1002/qj.828.

[88] M. Kanamitsu, W. Ebisuzaki, J. Woollen *et al.*, "NCEP–DOE AMIP-II Reanalysis (R-2)", *Bulletin of the American Meteorological Society*, vol. 83, no. 11, pp. 1631–1643, 2002. DOI: 10.1175/BAMS-83-11-1631.

[89] European Centre for Medium-Range Weather Forecasts. (2018). ERA-Interim dataset, [Online]. Available: https://www.ecmwf.int/en/forecasts/datasets/archive-datasets/reanalysis-datasets/era-interim (visited on 19/02/2019).

[90] NOAA/ESRL/PSD. (2018). NCEP-DOE Reanalysis 2 dataset, [Online]. Available: https://www.esrl.noaa.gov/psd/data/gridded/data.ncep.reanalysis2.html (visited on 19/02/2019).

[91] D. A. Zappalà, M. Barreiro and C. Masoller, "Global atmospheric dynamics investigated by using Hilbert frequency analysis", *Entropy*, vol. 18, no. 11, p. 408, 2016. DOI: 10.3390/e18110408.

[92] R. F. Adler, G. J. Huffman, A. Chang *et al.*, "The Version 2 Global Precipitation Climatology Project (GPCP) Monthly Precipitation Analysis (1979-Present)", *Journal of Hydrometeorology*, vol. 4, no. 6, pp. 1147–1167, 2003.

[93] D. A. Zappalà, M. Barreiro and C. Masoller, "Quantifying changes in spatial patterns of surface air temperature dynamics over several decades", *Earth System Dynamics*, vol. 9, no. 2, pp. 383–391, 2018. DOI: 10.5194/esd-9-383-2018.

[94] B. Liebmann, C. Vera, L. M. V. Carvalho *et al.*, "An Observed Trend in Central South American Precipitation", *Journal of Climate*, vol. 17, no. 22, pp. 4357–4367, 2004. DOI: 10.1175/3205.1.

[95] R. Fu, L. Yin, W. Li *et al.*, "Increased dry-season length over southern Amazonia in recent decades and its implication for future climate projection", *Proceedings of the National Academy of Sciences*, vol. 110, no. 45, pp. 18 110–18 115, 2013. DOI: 10.1073/pnas.1302584110.

[96] G. Gu, R. F. Adler and G. J. Huffman, "Long-term changes/trends in surface temperature and precipitation during the satellite era (1979–2012)", *Climate Dynamics*, vol. 46, no. 3-4, pp. 1091–1105, 2016. DOI: 10.1007/s00382-015-2634-x.

[97] M. Yoshimori and A. J. Broccoli, "Equilibrium Response of an Atmosphere–Mixed Layer Ocean Model to Different Radiative Forcing Agents: Global and Zonal Mean Response", *Journal of Climate*, vol. 21, no. 17, pp. 4399–4423, 2008. DOI: 10.1175/2008JCLI2172.1.

[98] S. M. Kang, D. M. W. Frierson and I. M. Held, "The tropical response to extratropical thermal forcing in an idealized GCM: The importance of radiative feedbacks and convective parameterization", *Journal of the Atmospheric Sciences*, vol. 66, no. 9, pp. 2812–2827, 2009. DOI: 10.1175/2009JAS2924.1.

[99] D. M. W. Frierson and Y.-T. Hwang, "Extratropical influence on ITCZ shifts in slab ocean simulations of global warming", *Journal of Climate*, vol. 25, no. 2, pp. 720–733, 2012. DOI: 10.1175/JCLI-D-11-00116.1.

[100] T. Schneider, T. Bischoff and G. H. Haug, "Migrations and dynamics of the intertropical convergence zone", *Nature*, vol. 513, no. 7516, pp. 45–53, 2014. DOI: 10.1038/nature13636.

[101] S. Talento and M. Barreiro, "Simulated sensitivity of the tropical climate to extratropical thermal forcing: tropical SSTs and African land surface", *Climate Dynamics*, vol. 47, no. 3–4, pp. 1091–1110, 2016. DOI: 10.1007/s00382-015-2890-9.

[102] D. A. Zappalà, M. Barreiro and C. Masoller, "Uncovering temporal regularity in atmospheric dynamics through Hilbert phase analysis", *arXiv*, 2019. [Online]. Available: https://arxiv.org/abs/1902.04458.

[103] K. Hasselmann, "Stochastic climate models. Part I. Theory", *Tellus*, vol. 28, no. 6, pp. 473–485, 1976. DOI: 10.3402/tellusa.v28i6.11316.

[104] GCOS Working Group on Surface Pressure. (2018). Niño 3.4 SST index, [Online]. Available: https://www.esrl.noaa.gov/psd/gcos_wgsp/Timeseries/Data/nino34.long.anom.data (visited on 22/01/2019).

[105] D. Boigelot. (2011). An example of the correlation of x and y for various distributions of (x,y) pairs, [Online]. Available: https://en.wikipedia.org/wiki/File:Correlation_examples2.svg (visited on 22/01/2019).

[106] M. Paluš, "From nonlinearity to causality: statistical testing and inference of physical mechanisms underlying complex dynamics", *Contemporary Physics*, vol. 48, no. 6, pp. 307–348, 2007. DOI: 10.1080/00107510801959206.

[107] G. Lancaster, D. Iatsenko, A. Pidde *et al.*, "Surrogate data for hypothesis testing of physical systems", *Physics Reports*, vol. 748, pp. 1–60, 2018. DOI: 10.1016/j.physrep.2018.06.001.

[108] J. Hlinka, D. Hartman, M. Vejmelka *et al.*, "Non-linear dependence and teleconnections in climate data: sources, relevance, nonstationarity", *Climate Dynamics*, vol. 42, no. 7–8, pp. 1873–1886, 2014. DOI: 10.1007/s00382-013-1780-2.

[109] J. I. Deza, C. Masoller and M. Barreiro, "Assessing the direction of climate interactions by means of complex networks and information theoretic tools", *Chaos*, vol. 25, p. 033 105, 2015. DOI: 10.1063/1.4914101.

[110] Y. Wang, A. Gozolchiani, Y. Ashkenazy *et al.*, "Dominant Imprint of Rossby Waves in the Climate Network", *Physical Review Letters*, vol. 111, p. 138 501, 2013. DOI: 10.1103/PhysRevLett.111.138501.

Publications

1. Dario A. Zappalà, Marcelo Barreiro and Cristina Masoller.
   Global atmospheric dynamics investigated by using Hilbert frequency analysis.
   Entropy, 18, 408 (2016).

2. Dario A. Zappalà, Marcelo Barreiro and Cristina Masoller.
   Quantifying changes in spatial patterns of surface air temperature dynamics over several decades.
   Earth Syst. Dynam., 9, 383–391 (2018).

3. Dario A. Zappalà, Marcelo Barreiro and Cristina Masoller.
   Uncovering temporal regularity in atmospheric dynamics through Hilbert phase analysis.
   Submitted (2019). Preprint available at `https://arxiv.org/abs/1902.04458`.

4. Dario A. Zappalà, Marcelo Barreiro and Cristina Masoller.
   A Hilbert approach to investigate climate connectivity.
   In preparation.

Other publications not related to this thesis

1. Dario A. Zappalà, Alessandro Pluchino, Andrea Rapisarda.
   Selective altruism in collective games.
   Physica A, 410, 496–512 (2014).

Conferences, workshops and research stays

- **XXXV Dynamics Days Europe 2015**
  Exeter (United Kingdom), 6–10 september 2015.
  Poster: "Investigating phase dynamics and synchronisation in climate data".

- **XX Congreso de Física Estadística**
  Badajoz (Spain), 5–7 October 2015.
  Poster: "Investigating phase dynamics and synchronisation in climate data".

- **Advanced Course on Applied Paleoclimate Time Series Analysis**
  Heckenbeck (Germany), 21–25 September 2015.
  Course on climate time series analysis held by Dr. Manfred Mudelsee.

- **Jornada de Investigadores Predoctorales Interdisciplinaria 2016**
  Barcelona (Spain), 2 February 2016.
  Poster: "Investigating dynamics and synchronisation in climate data".

- **EGU General Assembly 2016**
  Vienna (Austria), 17–22 April 2016.
  Poster: "Investigating Hilbert frequency dynamics and synchronisation in climate data".

- **V Jornada complexitat.cat**
  Barcelona (Spain), 19 May 2016.
  Poster: "Investigating Hilbert frequency dynamics and synchronisation in climate data".

- **NoLineal 2016**
  Sevilla (Spain), 7–10 June 2016.
  Talk: "Investigating Hilbert frequency dynamics and synchronisation in climate data".

- **30 Years of Nonlinear Dynamics in Geosciences**
  Rhodes (Greece), 3–8 July 2016.
  Talk: "Investigating Hilbert frequency dynamics and synchronisation in climate data".

- **IberSinc**
  Tarragona (Spain), 6–7 October 2016.
  Talk: "Characterising atmospheric dynamics and synchronisation in climate data".

- **Research stay at Montevideo**
  Universidad de la República, Montevideo (Uruguay), 6–22 February 2017.
  Collaboration with professor Marcelo Barreiro. Research work published in [93].

- **XXI Congreso de Física Estadística**
  Sevilla (Spain), 30 March – 1 April 2017.
  Poster: "Unveiling signatures of interdecadal climate changes by Hilbert analysis".

- **EGU General Assembly 2017**
  Vienna (Austria), 23–25 April 2017.
  Talk: "Unveiling signatures of interdecadal climate changes by Hilbert analysis".

- **Crossroads in Complex Systems**
  Palma de Mallorca (Spain), 5–8 June 2017.
  Poster: "Unveiling signatures of interdecadal climate changes by Hilbert analysis".

- **Data Science and Environment**
  Brest (France), 3–6 July 2017.
  Conference and workshop.
  Poster: "Unveiling signatures of interdecadal climate changes by Hilbert analysis".

- **BIFI International Conference 2018**
  Zaragoza (Spain), 6–8 February 2018.
  Poster: "Quantifying phase synchronisation and connectivity in surface air temperature data".

- **EGU General Assembly 2018**
  Vienna (Austria), 8–13 April 2018.
  Posters: "Characterising surface air temperature dynamics using Hilbert transform", "Quantifying phase synchronisation and connectivity in surface air temperature data".

- **Predicting Transitions in Complex Systems**
  Dresden (Germany), 23–27 Abril 2018.
  Talk: "Quantifying changes in spatial patterns of surface air temperature dynamics over several decades".

- **Nonlinear Dynamics of Electronic Systems**
  Acireale (Italy), 11–13 June 2018.
  Talk: "A Hilbert approach to investigate climate connectivity".

- **XXII Congreso de Física Estadística**
  Madrid (Spain), 18–20 October 2018.
  Poster: "A Hilbert approach to investigate climate connectivity".
  Awarded as one of the five best posters.

- **XIV Jornada de Recerca del Departament de Física**
  Barcelona (Spain), 29 January 2019.
  Poster: "A Hilbert approach to investigate climate connectivity".